Asian Journal of Physical and Chemical Sciences

3(4): 1-33, 2017; Article no.AJOPACS.37462
ISSN: 2456-7779

Spectral Method Applied to Chemical Non-Equilibrium Reentry Flows in 2D: Five Species – High Order Analysis

Edisson Sávio de Góes Maciel[1*] and Cláudia Regina de Andrade[2]

[1]Instituto Tecnológico de Aeronáutica (ITA), Rua Santa Clara, 245 – Cx. Postal: 2029, 12.243-970 – São José dos Campos, SP, Brazil.
[2]Instituto Tecnológico de Aeronáutica (ITA), Praça Mal. do Ar Eduardo Gomes, 50 – 12.228-900 – São José dos Campos, SP, Brazil.

Authors' contributions

This work was carried out in collaboration between both authors. Author ESDGM designed the study, performed the statistical analysis, wrote the protocol, wrote the first draft of the manuscript and managed the analyses of the study. Author CRDA managed the literature searches. Both authors read and approved the final manuscript.

Article Information

DOI: 10.9734/AJOPACS/2017/37462
Editor(s):
(1) Hesham Mansour, Physics Department, Faculty of Science, Cairo University, Egypt.
Reviewers:
(1) Jagdish Prakash, University of Botswana, Botswana.
(2) Francisco Bulnes, Mexico.
Complete Peer review History: http://www.sciencedomain.org/review-history/21788

Original Research Article

Received 18th October 2017
Accepted 3rd November 2017
Published 7th November 2017

ABSTRACT

In the present work, a study involving a spectral method to solve the reactive Euler and Navier-Stokes equations is performed. The Euler and Navier-Stokes equations, in conservative and finite volume contexts, employing structured spatial discretization, on a condition of chemical non-equilibrium, are studied. The spectral method presented in this work employs collocation points and variants of Chebyshev and Legendre interpolation functions are analyzed. High-order studies are performed to verify the accuracy of the spectral method. The "hot gas" hypersonic flows around a blunt body, around a double ellipse, and around a reentry capsule in two-dimensions are performed. The Van Leer and the Liou and Steffen Jr. flux vector splitting algorithms are applied to accomplish the numerical experiments. The Euler backward integration method is employed to march the schemes in time. The convergence process is accelerated to steady state condition

**Corresponding author: E-mail: edissonsavio@yahoo.com.br;*

through a spatially variable time step procedure, which has proved effective gains in terms of computational acceleration (see Maciel). The reactive simulations involve Earth atmosphere chemical model of five species and seventeen reactions, based on the Saxena and Nair model. N, O, N_2, O_2, and NO species are used to perform the numerical comparisons. The results have indicated that the Chebyshev collocation point variants are more accurate in terms of stagnation pressure estimations, whereas the Legendre collocation point variants are more accurate in terms of the lift coefficient estimations. Moreover, the Legendre collocation point variants are more computationally efficient and cheaper.

Keywords: Hypersonic flow; chemical non-equilibrium reentry flows; reactive Euler and Navier-Stokes equations; high order accuracy; Van Leer scheme; Liou and Steffen Jr. scheme; spectral method.

1. INTRODUCTION

There are several approaches for computationally modeling fluid dynamics. These include finite difference, finite element, and spectral methods to name a few. Finite element and finite difference methods are frequently used and offer a wide range of well-known numerical schemes. These schemes can vary in terms of computational accuracy but are typically of lower order of accuracy. If a more accurate solution is desired, it is common practice to refine the mesh either globally or in a region of interest. This can often be a complicated or time consuming process as global mesh refinement will greatly increase the computation time while local refinement requires an elaborated refinement operation, [1].

Alternatively, polynomial refinement has been used to improve the solution accuracy and has been shown to converge more quickly than mesh refinement in some cases [2-3]. For finite difference methods, polynomial refinement is performed by including neighboring node values in a higher order polynomial [4]. This can increase the complexity of the scheme especially near the boundaries where nodes do not exist to construct the higher order polynomials. Finite element methods instead increase the number of unknown values within the cell itself to construct a higher order solution [5].

A scheme with a very high formal order of accuracy will not necessarily always produce the highest resolution. [6] demonstrated that a spectral-like scheme with a formal fourth-order accuracy produced a much more highly resolved solution than schemes with higher formal orders of accuracy when comparing modified wave numbers. Therefore, formal order of accuracy does not provide a comprehensive basis for selecting the best solution procedure. State-of-art methods such as spectral methods fall into this category.

Spectral methods are considered a class of solution techniques using sets of known functions to solve differential equations [7]. Such methods are generally considered high order and capable of obtaining solutions with a high resolution. Unlike finite-difference and finite-element methods, spectral methods utilize an expansion in terms of global, rather than local, basis functions to represent the solution of a differential equation. When properly applied, these techniques accurately resolve phenomena on the scale of the mesh spacing. The order of truncation error decay with mesh refinement is also higher than which can be achieved with finite-difference and finite-element methods. For problems with smooth solutions, it is possible to produce spectral method whose truncation error goes to zero as faster than any finite power of the mesh spacing (exponential convergence).

Spectral methods may be viewed as an extreme development of the class of discretization schemes known by the generic name of method of weighted residuals (MWR) [8]. The key elements of the MWR are the trial functions (also called the expansion or approximating functions) and the test functions (also known as weighted functions). The trial functions are used as the basis functions for a truncated series expansion of the solution that, when substituted into the differential equation, produces the residual. The test functions are used to enforce the minimization of the residual.

The choice of the trial functions is what distinguishes the spectral methods from the element and finite difference methods. The trial functions for spectral methods are infinitely differentiable global functions (Typically, they are tensor products of the eigenfunctions of singular

Sturm-Liouville problems). In the case of finite element methods, the domain is divided into small elements and a trial function is specified in each element. The trial functions are thus local in character and well suited for handling complex geometries. The finite difference trial functions are likewise local.

The choice of test function distinguishes between Galerkin and collocation approaches. In the Galerkin approach, the test functions are the same as the trial functions, whereas in the collocation approach the test functions are translated Dirac delta functions. In other words, the Galerkin approach is equivalent to a least-square approximation, whereas the collocation approach requires the differential equations to be solved exactly at the collocation points.

The collocation approach is the simplest of the MWR and appears to have been first used by [9] in his study of electronic energy bands in metals. A few years later, [10] applied this method to the problem of torsion in square prism. [11] developed it as a general method for solving ordinary differential equations. They used a variety of trials functions and an arbitrary distribution of collocation points. The work of [12] established for the first time that a proper choice of the trial functions and the distribution of collocation points are crucial to the accuracy of the solution. Perhaps he should be credited with laying down the foundation of the orthogonal collocation method.

Spectral methods have been used on one-dimensional, compressible flow problems with piecewise linear solutions by [13-14]. These reports demonstrated that spectral methods, when combined with appropriate filtering techniques, can capture one-dimensional shock waves in otherwise featureless flows. A different sort of demonstration was provided by [15]. They exhibited spectral solutions of compressible flows with nontrivial structures in the smooth regions.

Renewed interest in the area of hypersonic flight has brought Computational Fluid Dynamics (CFD) to the forefront of fluid flow research [16]. Many years have seen a quantum leap in advancements made in the areas of computer systems and software which utilize them for problem solving. Sophisticated and accurate numerical algorithms are devised routinely that are capable of handling complex computational problems. Experimental test facilities capable of addressing complicated high-speed flow problems are still scarce because they are too expensive to build and sophisticated measurements techniques appropriate for such problems, such as the non-intrusive laser, are still in the development stage. As a result, CFD has become a vital tool in the flow problem solution.

In high speed flows, any adjustment of chemical composition or thermodynamic equilibrium to a change in local environment requires certain time. This is because the redistribution of chemical species and internal energies require certain number of molecular collisions, and hence a certain characteristic time. Chemical non-equilibrium occurs when the characteristic time for the chemical reactions to reach local equilibrium is of the same order as the characteristic time of the fluid flow. Similarly, thermal non-equilibrium occurs when the characteristic time for translation and various internal energy modes to reach local equilibrium is of the same order as the characteristic time of the fluid flow. Since chemical and thermal changes are the results of collisions between the constituent particles, non-equilibrium effects prevail in high-speed flows in low-density air.

In chemical non-equilibrium flows the mass conservation equation is applied to each of the constituent species in the gas mixture. Therefore, the overall mass conservation equation is replaced by as many species conservation equations as the number of chemical species considered. The assumption of thermal non-equilibrium introduces additional energy conservation equations – one for every additional energy mode. Thus, the number of governing equations for non-equilibrium flow is much bigger compared to those for perfect gas flow. A complete set of governing equations for non-equilibrium flow may be found in [17-18].

In the present work, a study involving a spectral method to solve the reactive Euler and Navier-Stokes equations is performed. The Euler and Navier-Stokes equations, in conservative and finite volume contexts, employing structured spatial discretization, on a condition of chemical non-equilibrium, are studied. The spectral method presented in this work employs collocation points and variants of Chebyshev and Legendre interpolation functions are analyzed. High-order studies are performed to verify the accuracy of the spectral method. The “hot gas” hypersonic flows around a blunt body, around a double ellipse, and around a reentry capsule in

two-dimensions are performed. The [19-20] flux vector splitting algorithms are applied to accomplish the numerical experiments. The Euler backward integration method is employed to march the schemes in time. The convergence process is accelerated to steady state condition through a spatially variable time step procedure, which has proved effective gains in terms of computational acceleration (see [21-22]). The reactive simulations involve Earth atmosphere chemical model of five species and seventeen reactions, based on the [23] model. N, O, N_2, O_2, and NO species are used to perform the numerical comparisons. The results have indicated that the Chebyshev collocation point variants are more accurate in terms of stagnation pressure estimations, whereas the Legendre collocation point variants are more accurate in terms of the lift coefficient estimations. Moreover, the Legendre collocation point variants are more computationally efficient and cheaper.

2. SPECTRAL METHOD

Two classes of techniques for spectral discretization are referred to as tau and collocation methods [24]. The latter technique is used here. In this scheme, the approximation series is determined by satisfying the differential equation exactly at a set of distinct collocation points. The locations of these points in the domain are linked to the choice of basis function. In this study, arbitrary collocation points are implemented. The collocation method is used here since enforcement of boundary conditions and evaluations of nonlinear terms are straightforward. Additionally, some accuracy advantage is seen in the collocation method over the tau method for a number of problems [24]. The series expansion for a function Q(x) may be represented as

$$Q_N(x) = \sum_{n=0}^{N} \hat{Q}_n B_n(x), \tag{1}$$

where $B_n(x)$ are the basis functions and N is the total number of nodes employed in the interpolation process (it is also the order of accuracy of the spectral method). The coefficients $\hat{Q}_n$ are often termed the spectrum of $Q_N(x)$. One common technique used to evaluate the spectrum is to consider Eq. (1) as an interpolation series representing Q(x). The interpolation "nodes" of such series are the collocation points of the method. For a scheme based on Chebyshev collocation, the basis functions are:

$$B_n(x) = T_n(x) = 2xP_{n-1}(x) - P_{n-2}(x), \quad n \geq 2, \tag{2}$$

with: $P_0(x) = 1$ and $P_1(x) = x$. The Chebyshev-Gauss-Lobatto standard collocation points are

$$x_l = \cos\left(\frac{\pi l}{N}\right), \qquad l = 0, 1, \ldots, N. \tag{3}$$

The Chebyshev collocation points result from a simple change of variables, which relates the Chebyshev interpolation series to a Fourier cosine series [24]. To evaluate the $\hat{Q}_n$, the inverse relation is required. This is

$$\hat{Q}_n = \hat{c}_n \sum_{l=0}^{N} w_l B_n(x_l) Q_{i,j}, \qquad n = 0, 1, \ldots, N, \tag{4}$$

with w_l being a normalized weighting function and $\hat{c}_n$ a constant. These variables assume the following expressions to a Chebyshev-Gauss-Lobatto interpolation:

$$\hat{c}_n = \frac{2}{N\bar{c}_n}, \quad \text{where:} \quad \bar{c}_n = \begin{cases} 2, & n = 0 \text{ or } N \\ 1, & 1 < n < N-1 \end{cases};$$

$$\text{and} \quad w_l = \frac{1}{\bar{c}_l}. \tag{5}$$

Legendre collocation is based on using Legendre polynomials as the basis function in Eq. (1), e.g.,

$$B_n(x) = \left[(2n-1)xP_{n-1}(x) - (n-1)P_{n-2}(x)\right]/n, \quad n \geq 2, \tag{6}$$

where: $P_0(x) = 1$ and $P_1(x) = x$. Interpolation via Legendre series cannot easily be related to trigonometric interpolation, so there is no simple expression to evaluate the $\hat{Q}_n$ coefficients. Appeal must be made to the theory of numerical quadrature to form an approximation to the integrals which result from analytic Legendre interpolation [25]. Considering Eq. (4), the normalized weights and constant of the Legendre-Gauss-Lobatto collocation points are:

$$w_l = \frac{1}{N(N+1)B_N^2(x_l)} \quad \text{and}$$

$$\hat{c}_n = \begin{cases} 2n+1, & n = 0,1,...,N-1 \\ N, & n = N \end{cases}. \tag{7}$$

In this work, it was assumed that the Legendre-Gauss-Lobatto collocation points are the same as the Chebyshev-Gauss-Lobatto ones. It was also adopted the following collocation points and normalized weight for the Chebyshev-Gauss-Radau interpolation, based on the work of [26]:

$$x_l = \cos\left(\frac{2\pi l}{2N+1}\right), \tag{8}$$

$$w_l = \begin{cases} \frac{N}{2N+1}, & l = 0 \\ \frac{N}{N+1}, & \text{elsewhere} \end{cases}. \tag{9}$$

For the Legendre-Gauss-Radau interpolation, also based in [26], the collocation points are defined by Eq. (8) and the normalized weights are described by:

$$w_l = \begin{cases} \frac{1}{(N+1)^2}, & l = 0 \\ \frac{1}{2(N+1)^2} \times \frac{1-x_l}{B_N(x_l)}, & \text{elsewhere} \end{cases}. \tag{10}$$

The same calculation to the vector of conserved variables Q is applied to the vector of flux C, to be defined in section 4.

Hence, we have two collocation point options and two normalized weight functions to be considered by the Chebyshev and the Legendre methods, namely: Chebyshev-Gauss-Radau, Chebyshev-Gauss-Lobatto, Legendre-Gauss-Radau and Legendre-Gauss-Lobatto.

3. EULER AND NAVIER-STOKES EQUATIONS

As the Navier-Stokes equations tend to the Euler equations when high Reynolds number are employed, only the former equations are presented. The reactive Navier-Stokes equations in chemical non-equilibrium were implemented on a finite volume context, in the two-dimensional space. In this case, these equations in integral and conservative forms can be expressed by:

$$\frac{\partial}{\partial t}\int_V Q dV + \int_S \vec{F} \bullet \vec{n} dS = \int_V S_C dV \text{, with:}$$

$$\vec{F} = (E_e - E_v)\vec{i} + (F_e - F_v)\vec{j}, \tag{11}$$

where: Q is the vector of conserved variables, V is the volume of a computational cell, $\vec{F}$ is the complete flux vector, $\vec{n}$ is the unity vector normal to the flux face, S is the flux area, S_C is the chemical source term, E_e and F_e are the convective flux vectors or the Euler flux vectors in the x and y directions, respectively, and E_v and F_v are the viscous flux vectors in the x and y directions, respectively. For expressions to calculate the flux area see Table 1. The $\vec{i}$ and $\vec{j}$ unity vectors define the Cartesian coordinate system. Eight (8) conservation equations are solved: one of general mass conservation, two of linear momentum conservation, one of total energy, and four of species mass conservation. Therefore, one of the species is absent of the iterative process. The CFD (Computational Fluid Dynamics) literature recommends that the species of biggest mass fraction of the gaseous mixture should be omitted, aiming to result in a minor numerical accumulation error, corresponding to the biggest mixture constituent (in the case, the air). To the present study, in which is chosen a chemical model to the air composed of five (5) chemical species (N, O, N_2, O_2, and NO) and seventeen (17) chemical reactions, being fifteen (15) dissociation reactions (endothermic reactions) and two (2) of exchange or recombination, this species can be the N_2 or the O_2. To this work, it was chosen the N_2. The vectors Q, E_e, F_e, E_v, F_v and S_C as well their parameters are defined in [27-28]. Details of the present implementation for the five species chemical model, as well the specification of the thermodynamic and transport properties are described in [27-28].

4. FLUX VECTOR SPLITTING SCHEMES

Considering the two-dimensional and structured case, the two algorithms follow that described in [19-20,27-28], where a one-temperature model is taken into account. The algorithms are decomposed in two contributions, according to [29]: the dynamic and chemical contributions. Fig. 1 shows a schematic of the computational cell, its nodes, and flux interfaces. The time integration is performed employing the Euler backward method, first-order accurate in time, to

the two types of convective flux. Both schemes are first-order accurate in space and in time. The high-order spatial accuracy is obtained, in the current study, by the spectral method.

The viscous formulation follows that of [30], which adopts the Green theorem to calculate primitive variable gradients. The viscous gradients at the interface are obtained by arithmetical average between cell (i,j) and its neighbors. As was done with the convective terms, there is a need to separate the viscous flux in two parts: dynamical viscous flux, and chemical viscous flux. The dynamical part corresponds to the first four equations of the Navier-Stokes ones, and the chemical part corresponds to the following four equations.

5. SPATIALLY VARIABLE TIME STEP

The spatially variable time step has proved efficient gains in terms of convergence acceleration, as verified by [21-22]. The total pressure of the gaseous mixture is determined by Dalton law, which indicates that the total pressure of the gas is the sum of the partial pressure of each constituent gas, resulting in:

$$p_s = c_s \rho R_s T \quad \text{and} \quad p = \sum_{s=1}^{ns} p_s \,, \tag{12}$$

where: p_s is the species pressure, c_s is the mass fraction, ρ is the mixture density, R_s is the gas constant, T is the flow temperature, and "ns" is the total number of species. The speed of sound "a" to a reactive mixture is defined in [27-28]. Finally, the spatially variable time step is defined from the CFL (Courant-Friedrichs-Lewis) definition:

$$\Delta t_{i,j} = \frac{CFL \Delta s_{i,j}}{\sqrt{u_{i,j}^2 + v_{i,j}^2} + a_{i,j}}, \tag{13}$$

where $\Delta s_{i,j}$ is the characteristic length of each cell (defined between the minimum cell side and the minimum centroid distance between each cell and its neighbors), and $u_{i,j}$ and $v_{i,j}$ are the velocity components.

6. DIMENSIONLESS SCALES, INITIAL AND BOUNDARY CONDITIONS

6.1 Dimensionless Scales

The dimensionless employed to the chemical non-equilibrium case consisted in: R_s is nondimensionalized by a_{char}, where $a_{char} = \sqrt{\gamma p_{char} / \rho_{char}}$ and the characteristic properties are obtained from [31]; c_v, the specific heat at constant volume, is nondimensionalized by a_{char}; h_s and Δh_s^0, the enthalpy and the formation enthalpy, are nondimensionalized by a_{char}^2; T, translational/rotational temperature, is nondimensionalized by a_{char}; ρ_s and ρ are nondimensionalized by ρ_{char}; u and v are nondimensionalized by a_{char}; μ, the molecular viscosity, is nondimensionalized by μ_{char}; D, diffusion coefficient, nondimensionalized by a_{char}^2 dt_{char}, where dt_{char} is the minimum time step calculated in the computational domain at the first iteration; $\dot{\omega}$ is nondimensionalized by $(\rho_{char}/dt_{char})x10^{-3}$; e and p are nondimensionalized by $\rho_{char} a_{char}^2$.

6.2 Initial Condition

The initial conditions to the blunt body, to the double ellipse, and to the reentry capsule problems, for a five species chemical model, are presented in Tables. 2-4. The Reynolds number is obtained from data of [31].

6.3 Boundary Conditions

The boundary conditions are basically of four types: solid wall, entrance, exit, and continuity. These conditions are implemented with the help of ghost cells.

Wall condition: In inviscid case, this condition imposes the flow tangency at the solid wall. This condition is satisfied considering the wall tangent velocity component of the ghost volume as equals to the respective velocity component of its real neighbor cell. At the same way, the wall normal velocity component of the ghost cell is equaled in value, but with opposite signal, to the respective velocity component of the real neighbor cell. To the viscous case, the boundary condition imposes that the ghost cell velocity components be equal to the real cell velocity components, with the negative signal.

The normal pressure gradient of the fluid at the wall is assumed to be equal to zero according to a boundary-layer like condition. The same hypothesis is applied for the normal temperature gradient at the wall, assuming an adiabatic wall.

From the above considerations, density and translational / rotational temperature are extrapolated from the respective values of its real neighbor volume (zero order extrapolation). The mixture formation enthalpy is extrapolated from the real cell. To the species density, the non-catalytic condition is imposed, what corresponds to zero order extrapolation from the real cell.

Entrance condition: It is divided in two flow regimes:

(a) Subsonic flow: Three properties are specified and one extrapolated in the boundary conditions of the dynamic part of the [19-20] algorithms. This approach is based on information propagation analysis along characteristic directions in the calculation domain [32]. In other words, for subsonic flow, three characteristics propagate information pointing into the computational domain. Thus three flow properties must be fixed at the inlet plane. Just one characteristic line allows information to travel upstream. So, one flow variables must be extrapolated from the interior grid to the inlet boundary. The total energy was the extrapolated variable from the real neighbor volume, for the studied problems. Density and velocity components adopted values of the initial flow. To the chemical part, four information propagate upstream because it is assumed that all four equations are conducted by the eigenvalue "$(q_n$-a)". In the subsonic flow, all eigenvalues are negative and the information should be extrapolated.

(b) Supersonic flow: In this case no information travels upstream; therefore all variables are fixed with their initial values.

Exit condition: It is also divided in two flow regimes:

(a) Subsonic flow: Three characteristics propagate information outward the computational domain. Hence, the associated variables should be extrapolated from interior information. The characteristic direction associated to the "$(q_{normal}$-a)" velocity should be specified because it points inward to the computational domain [32]. In this case, the ghost volume total energy is specified from its initial value. Density and velocity components are extrapolated. To the chemical part, the eigenvalue "$(q_n$-a)" is again negative and the characteristic is always flowing in to the computational domain. Hence, the four chemical species under study should have their densities fixed by their initial values.

(b) Supersonic flow: All variables are extrapolated from interior grid cells, as no flow information can make its way upstream. In other words, nothing can be fixed.

Continuity condition: This condition imposes continuity of the flow at the trailing edge of the reentry capsule configuration. This is done considering the Kutta condition in this region. In terms of numerical implementation, it is obtained considering the vector of conserved variables above the wake as equal to the vector of conserved variables below the wake.

7. PHYSICAL PROBLEMS

Three physical problems were solved in this work, namely: blunt body, double ellipse, and reentry capsule. The first problem considers the geometry of a blunt body with 1.0 m of nose ratio and parallel rectilinear walls. The far field is located at 20.0 times the nose ratio in relation to the configuration nose. A mesh composed of 2,548 rectangular cells and 2,650 nodes was studied for the inviscid case, with an exponential stretching of 5.0% for the viscous case. This mesh is equivalent in finite differences to a one of 53x50 points. Fig. 2 shows the detail of the geometry and Figs. 3 and 4 exhibit the inviscid and viscous meshes.

The double ellipse problem is the second under study. The mesh is composed of 4,116 rectangular cells and 4,250 nodes, with an exponential stretching of 5.0% for the viscous case, and far field located at 20.0 unities. This mesh is equivalent in finite differences to a one of 85x50 points. Fig. 5 shows the double ellipse geometry and Figs. 6 and 7 exhibit the inviscid and viscous meshes.

The third problem is the geometry of the reentry capsule. Details of the configuration are presented in Fig. 8. The far field is also located at 20.0 unities. A mesh of 3,136 rectangular cells and 3,250 nodes was used for the inviscid case, whereas with an exponential stretching of 5.0% was used for the viscous simulations. This mesh is equivalent in finite differences to a one of 65x50 points. Figs. 9 and 10 show the inviscid and viscous meshes.

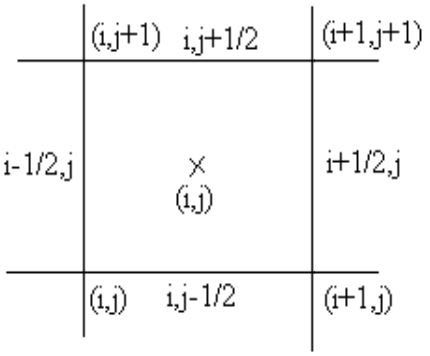

Fig. 1. Computational cell

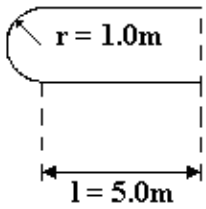

Fig. 2. Blunt body configuration

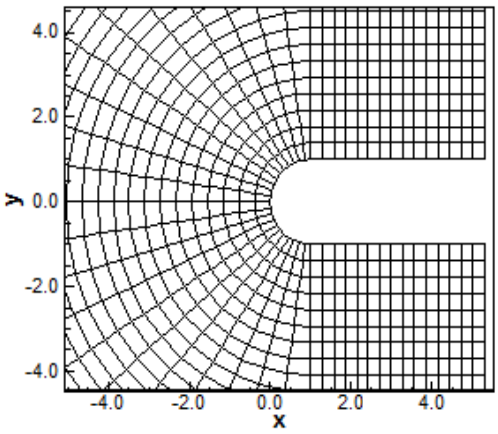

Fig. 3. Blunt body inviscid mesh

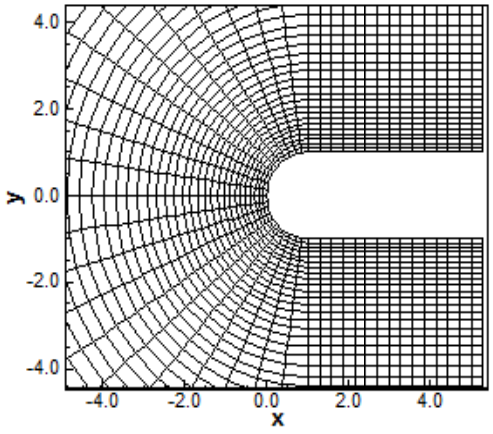

Fig. 4. Blunt body viscous mesh

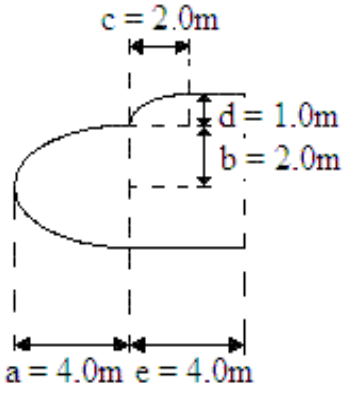

Fig. 5. Double ellipse configuration

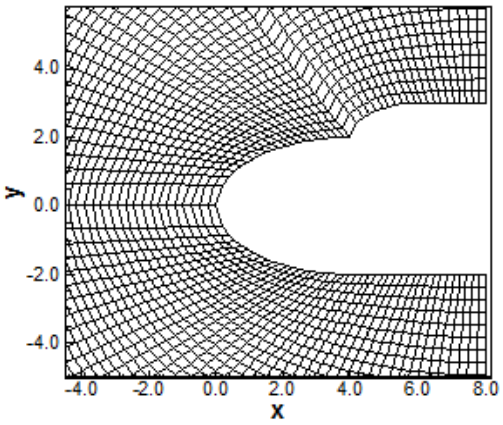

Fig. 6. Double ellipse inviscid mesh

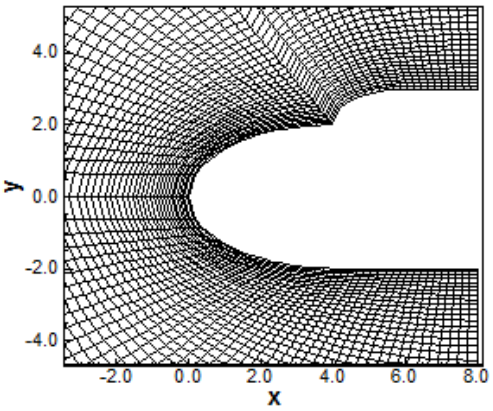

Fig. 7. Double ellipse viscous mesh

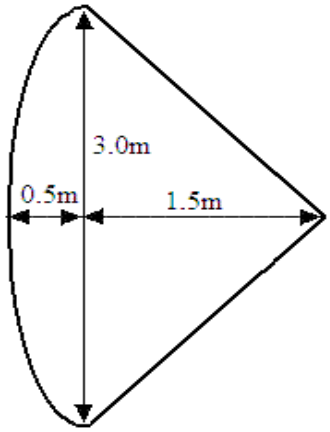

Fig. 8. Reentry capsule configuration

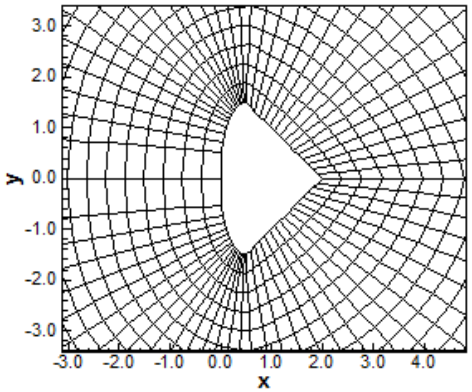

Fig. 9. Reentry capsule inviscid mesh

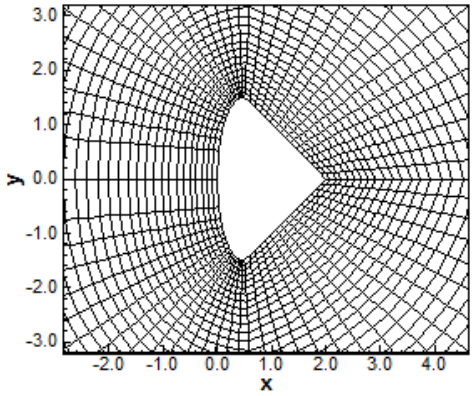

Fig. 10. Reentry capsule viscous mesh

BLUNT BODY INVISCID SOLUTIONS

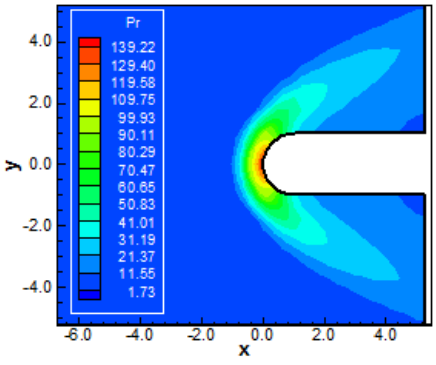

Fig. 11. Pressure contours (CGR-VL)

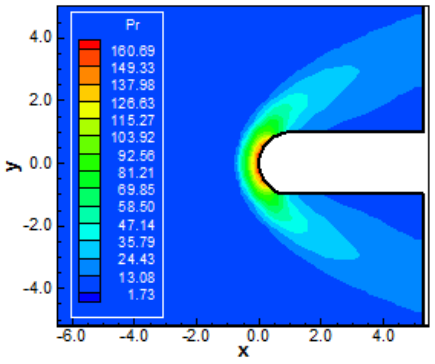

Fig. 12. Pressure contours (CGR-LS)

8. RESULTS

Tests were performed in a Core i7 processor of 2.1GHz and 8.0Gbytes of RAM microcomputer, in a Windows 7.0 environment. Three (3) orders of reduction of the maximum residual in the field were considered to obtain a converged solution. The residual was defined as the value of the discretized conservation equation. In the dynamic part of the flux vector splitting schemes, such definition results in:

$$\text{Residual} = -\Delta t_{i,j} / V_{i,j} \times C_{i,j}. \quad (14)$$

The attack angle was adopted equal to zero. For a matter of simplicity, we use the following abbreviations: Scheme [19] = VL; Scheme [20] = LS; Chebyshev-Gauss-Radau = CGR; Chebyshev-Gauss-Lobatto = CGL; Legendre-Gauss-Radau = LGR; and Legendre-Gauss-Lobatto = LGL. For the inviscid solutions, a 4th order spectral method was used, whereas in the viscous case, a 16th order spectral method was employed.

8.1 Blunt Body Problem

Inviscid case: Figs. 11 to 14 exhibit the pressure and temperature contours obtained by the VL and LS schemes as using the CGR collocation points. The LS algorithm captures a more intense shock than the VL scheme, as can be seen by the pressure contours. Good symmetry and homogenous properties are observed in the pressure and in the translational/rotational temperature contours. No pre-shock oscillations are observed. The maximum temperature at the configuration nose is 7,956.65K, obtained by the VL scheme.

Figs. 15 to 18 show the pressure and translational/rotational temperature contours generated by the VL and LS schemes as using CGL collocation points. The maximum pressure is obtained again by the LS algorithm, being inferior to that observed in the CGR case. Some pressure oscillations are observed close to the shock wave. The temperature contours presents good symmetry properties. The maximum temperature reaches the value of 8,115.91K and is again captured by the VL scheme. The contours are free of oscillations.

Figs. 19 to 22 present the pressure and translational/rotational temperature contours calculated by the VL and LS schemes when using the LGR collocation points. The pressure peaks of both solutions are smaller than those obtained in the Chebyshev variants. No pressure oscillations are observed and good symmetry properties are verified. The maximum temperature peak is 8,552.61K, obtained again by the VL scheme. Good symmetry properties are also observed in both contours.

Figs. 23 to 26 exhibit the pressure and temperature contours obtained by the VL and LS algorithms when using the LGL collocation points. The pressure peaks are still low. Good symmetry and homogeneous properties are observed and the shock wave is well captured. The temperature contours present also good symmetry properties, free of oscillations. The maximum temperature is obtained by the VL scheme with a value of 8,475.46K.

Viscous case: Figs. 27 to 30 present the pressure and temperature contours generated by the VL and LS schemes as using CGR collocation points. The pressure peaks are very close to the theoretical stagnation pressure value, with LS scheme being the closest. Good symmetry properties are observed and no pre-shock oscillations are observed. The maximum temperature is again calculated with the VL scheme, reaching the mark of 8,391.94K. Good symmetry properties are verified. Note that the heat transfer is better captured by the VL scheme, as can be seen by the contours of temperature close to the configuration wall. The correct transport of properties like viscosity and thermal conduction are qualitatively confirmed.

Figs. 31 to 34 show the pressure and translational/rotational temperature contours calculated by the VL and LS algorithms when using CGL collocation points. Again the LS' pressure peak is close to the theoretical value of stagnation pressure (see Table 5). The shock wave is well captured by both schemes, with pressure oscillations verified in the LS scheme close to the configuration nose. Figs. 33 and 34 show the translational/rotational temperature contours and the good transport of viscosity and thermal conduction is noted in the VL solution. The maximum temperature is 8,452.99 K and is again obtained by the VL scheme; in other words, the VL scheme is being more conservative than the LS scheme.

Figs. 35 to 38 exhibit the pressure and temperature contours obtained by the VL and LS algorithms as using the LGR collocation points. Both pressure contours are very similar in qualitative terms, although the pressure peaks are very low. Good symmetry properties are observed in both solutions, free of pre-shock oscillations. Figs. 37 and 38 exhibit the temperature contours calculated by the VL and LS schemes. The temperature field of LS algorithm is more intense than that of the VL scheme, reaching a maximum of 8,902.43K. Good symmetry and homogenous properties are observed in both figures.

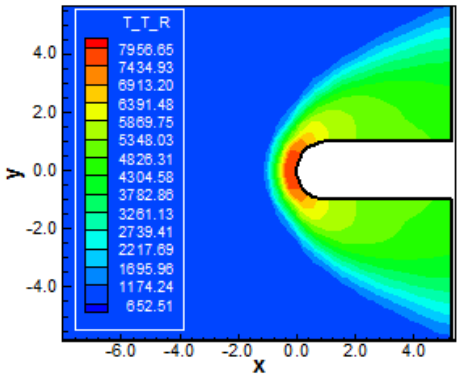

Fig. 13. Translational/rotational temperature contours (CGR-VL)

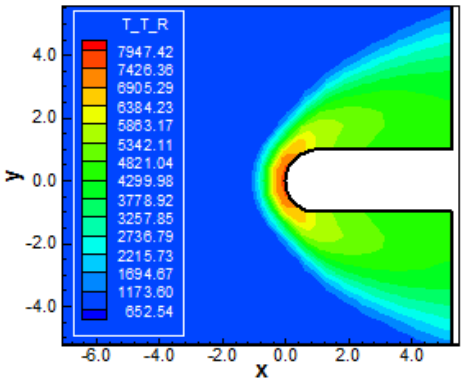

Fig. 14. Translational/rotational temperature contours (CGR-LS)

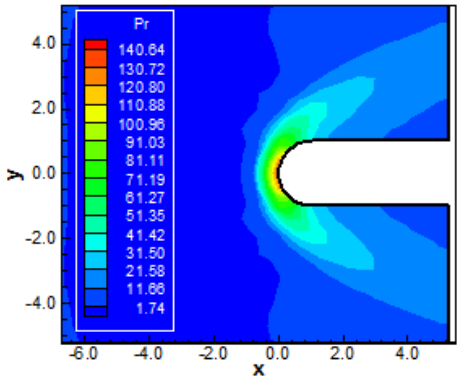

Fig. 15. Pressure contours (CGL-VL)

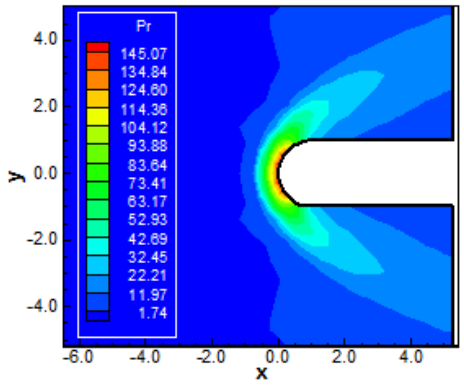

Fig. 16. Pressure contours (CGL-LS)

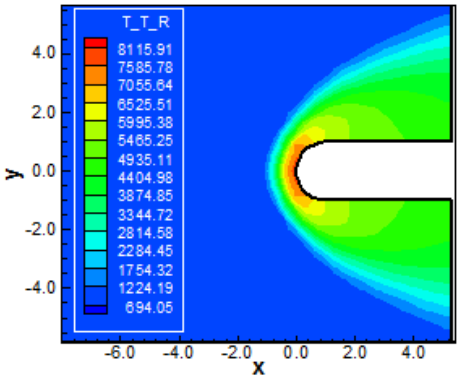

Fig. 17. Translational/rotational temperature contours (CGL-VL)

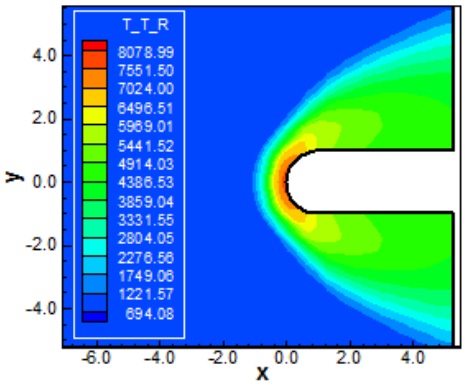

Fig. 18. Translational/rotational temperature contours (CGL-LS)

Figs. 39 to 42 present the pressure and translational/rotational temperature contours calculated by the VL and LS algorithms when using the LGL collocation points. Both pressures are reduced in relation to the theoretical stagnation pressure value. Both solutions present good symmetry and homogenous properties, free of oscillations. The shock waves are well captured and the transport of properties is well highlighted in the VL's temperature contours. The Legendre solutions present in general higher values to the stagnation temperature than the Chebyshev solutions. It seems that Chebyshev variants dominate the

pressure field, whereas the Legendre variants dominate the temperature field.

8.2 Double Ellipse

Inviscid case: In this problem, only the VL scheme converged in the numerical simulations. Figs. 43 to 50 show pressure and temperature contours generated by the VL and LS algorithms as using the CGR, CGL, LGR, and LGL collocation points. Comparing with the theoretical stagnation pressure value, the best result is due to CGR collocation points with an error of 3.79%. Good symmetry and homogenous properties are observed in all solutions and the two shock waves are well captured by all spectral variants.

Viscous case: Again, only the VL scheme generated converged results. Figs. 51 to 58 exhibit the pressure and temperature contours calculated with the VL and LS schemes as using the CGR, CGL, LGR, and LGL variants of the proposed spectral method. The best value to the stagnation pressure is captured by the CGR collocation points, with an error of 0.23%. Good symmetry and homogenous properties are observed in all solutions. Figs. 52, 54, 56 and 58 exhibit the thermal boundary layer captured by all variants of the spectral method as using the VL scheme. The transport properties are well detected by the VL scheme.

8.3 Reentry Capsule

Inviscid case: Figs. 59 to 62 present the pressure and translational/rotational temperature contours obtained by the VL and LS schemes as using the CGR collocation points. Figs. 59 and 60 present the pressure contours and good symmetry and homogenous properties are verified. The Kutta condition was correctly implemented. There are qualitative differences in the pressure contours captured by both schemes. The solution of Fig. 59 seems better to represent the normal shock. Figs. 61 and 62 present the temperature contours and good symmetry properties are noted. Again, the normal shock seems better captured by the VL solution.

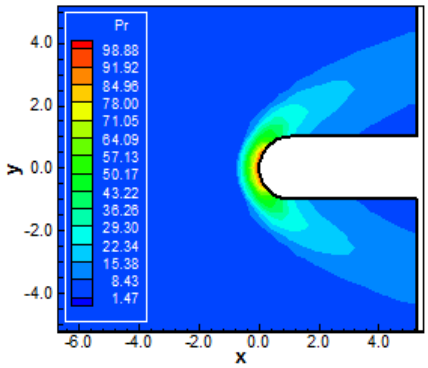

Fig. 19. Pressure contours (LGR-VL)

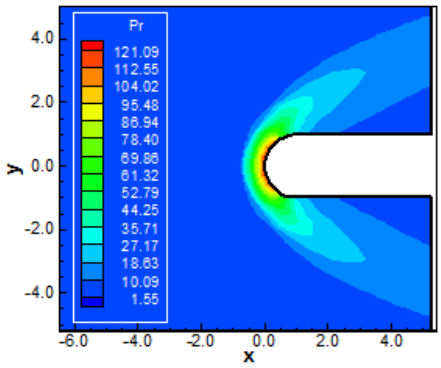

Fig. 20. Pressure contours (LGR-LS)

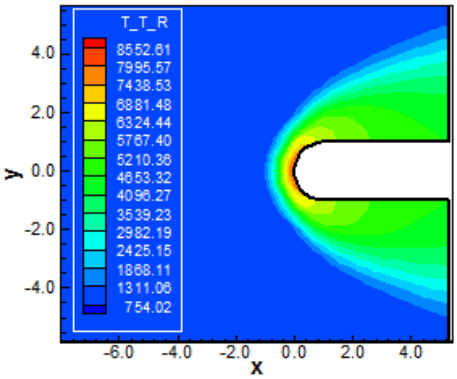

Fig. 21. Translational/rotational temperature contours (LGR-VL)

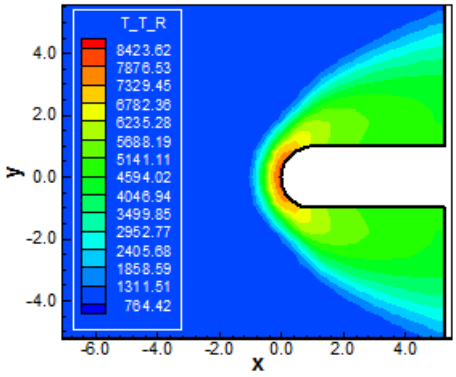

Fig. 22. Translational/rotationl temperature contours (LGR-LS)

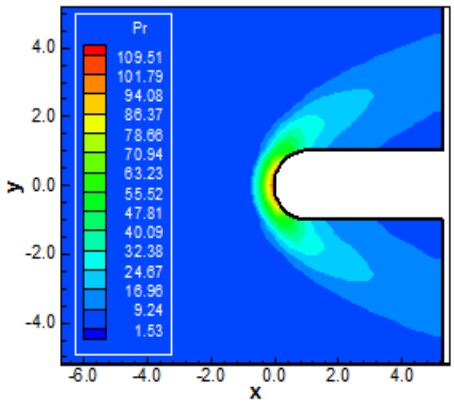

Fig. 23. Pressure contours (LGL-VL)

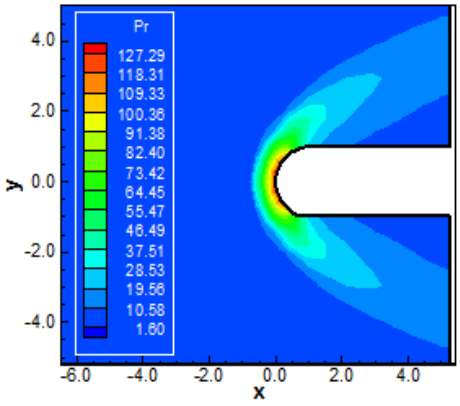

Fig. 24. Pressure contours (LGL-LS)

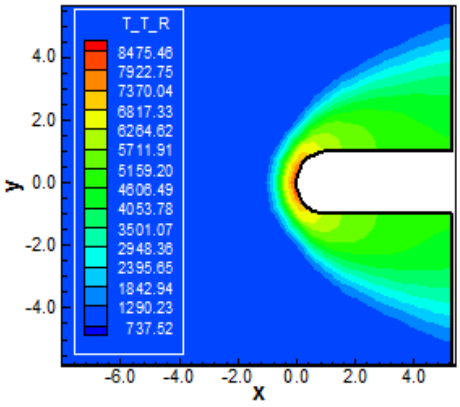

Fig. 25. Translational/rotational temperature contours (LGL-VL)

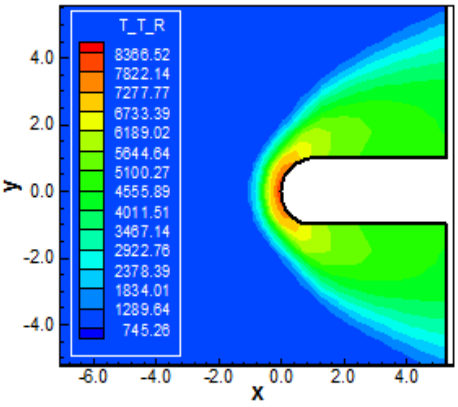

Fig. 26. Translational/rotational temperature contours (LGL-LS)

BLUNT BODY VISCOUS SOLUTIONS

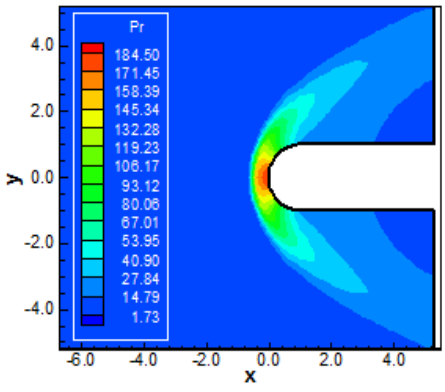

Fig. 27. Pressure contours (CGR-VL)

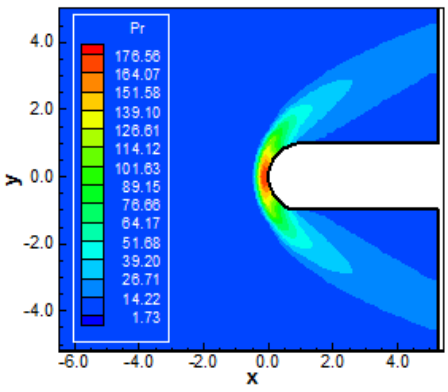

Fig. 28. Pressure contours (CGR-LS)

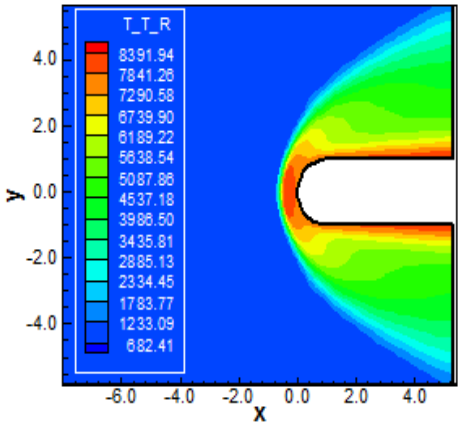

Fig. 29. Translational/rotational temperature contours (CGR-VL)

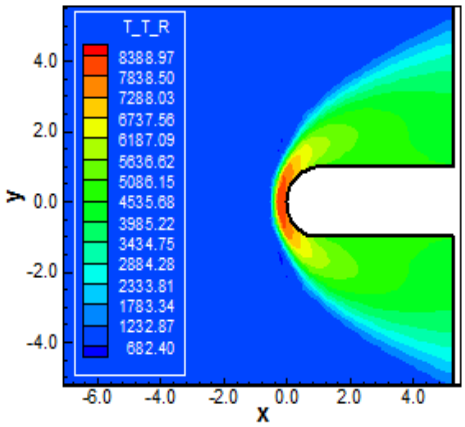

Fig. 30. Translational/rotational temperature contours (CGR-LS)

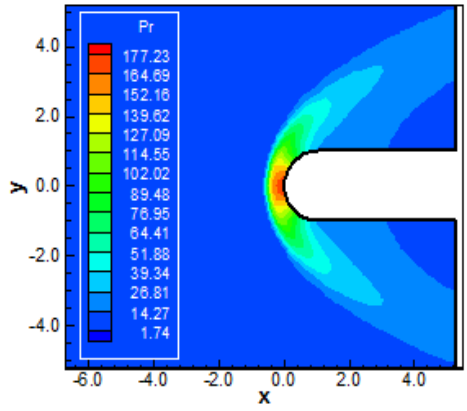

Fig. 31. Pressure contours (CGL-VL)

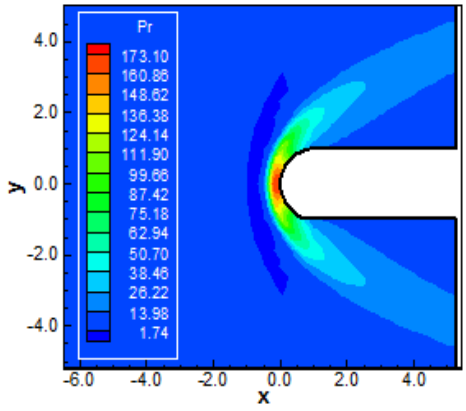

Fig. 32. Pressure contours (CGL-LS)

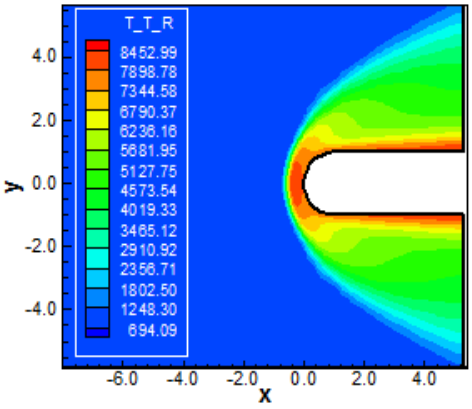

Fig. 33. Translational/rotational temperature contours (CGL-VL)

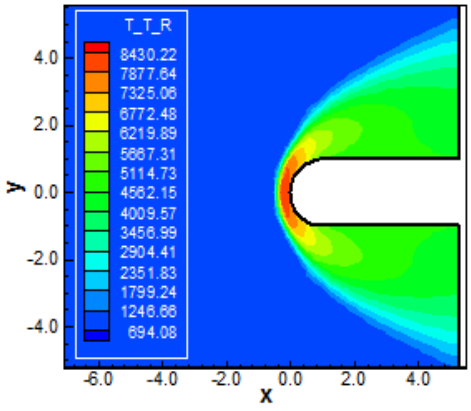

Fig. 34. Translational/rotational temperature contours (CGL-LS)

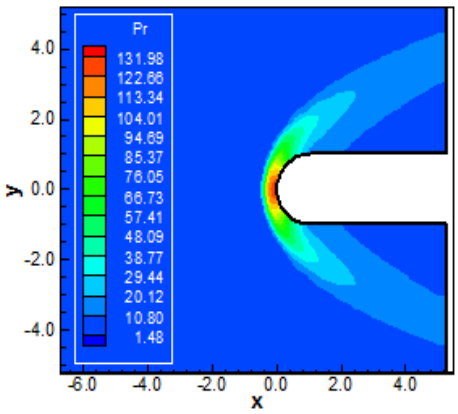

Fig. 35. Pressure contours (LGR-VL)

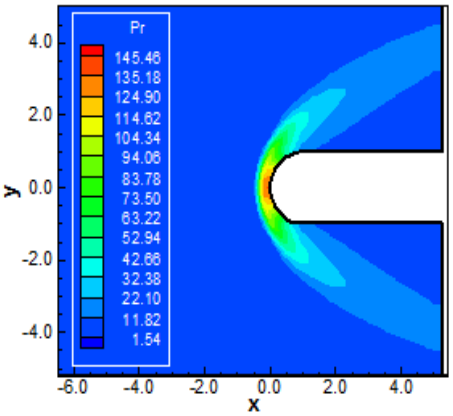

Fig. 36. Pressure contours (LGR-LS)

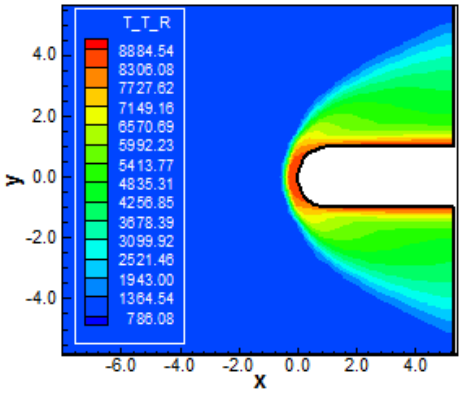

Fig. 37. Translational/rotational temperature contours (LGR-VL)

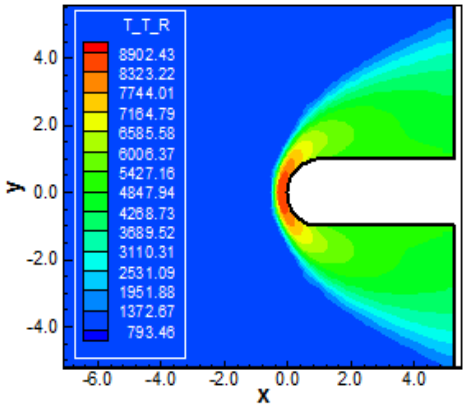

Fig. 38. Translational/rotational temperature contours (LGR-LS)

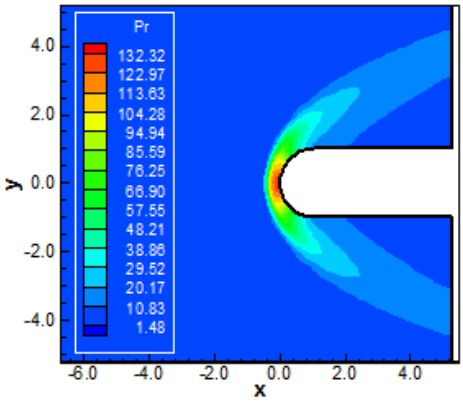

Fig. 39. Pressure contours (LGL-VL)

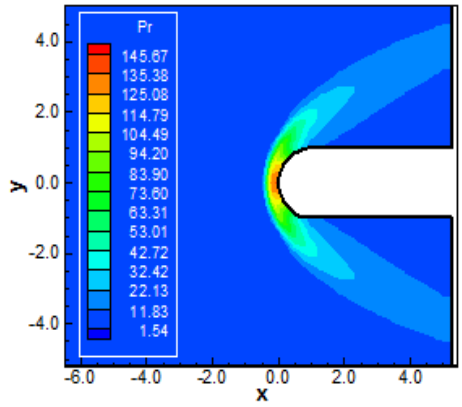

Fig. 40. Pressure contours (LGL-LS)

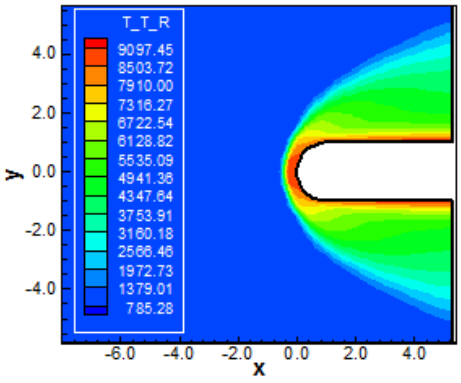

Fig. 41. Translational/rotational temperature contours (LGL-VL)

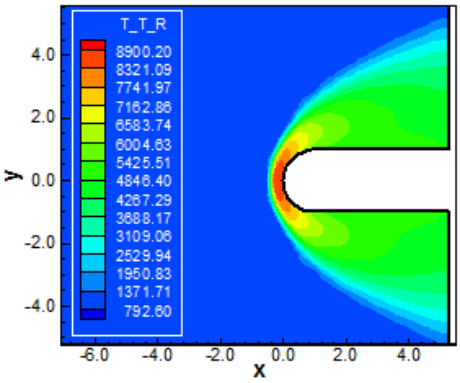

Fig. 42. Translational/rotational temperature contours (LGL-LS)

DOUBLE ELLIPSE INVISCID SOLUTIONS

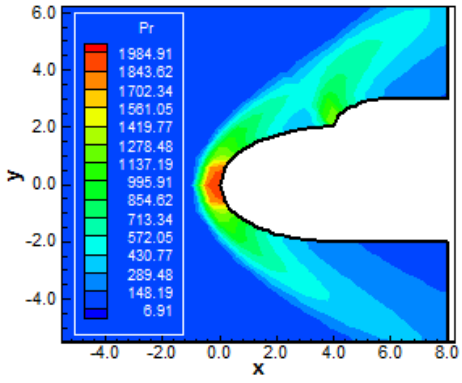

Fig. 43. Pressure contours (CGR-VL)

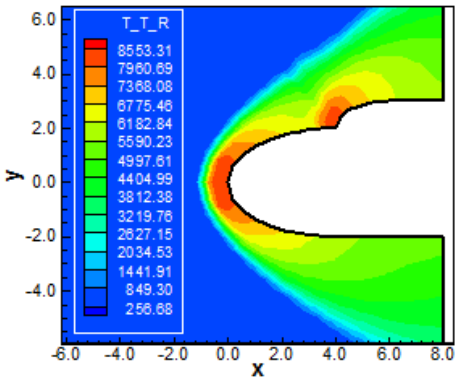

Fig. 44. Translational/rotational temperature contours (CGR-VL)

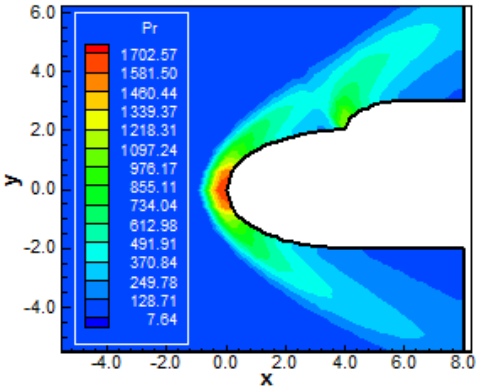

Fig. 45. Pressure contours (CGL-VL)

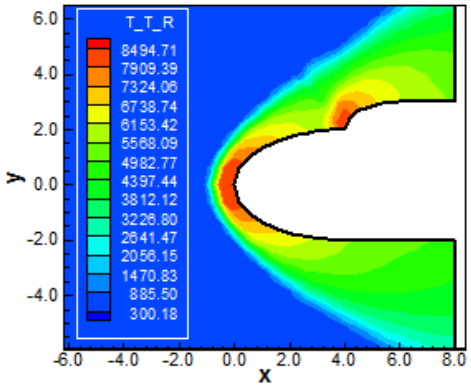

Fig. 46. Translational/rotational temperature contours (CGL-VL)

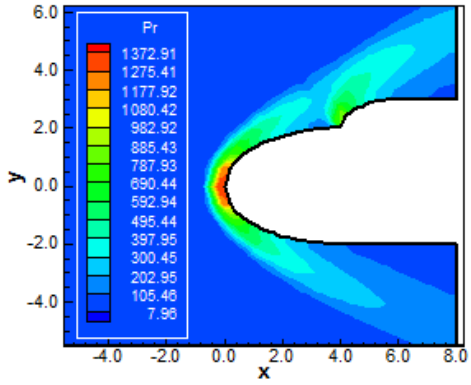

Fig. 47. Pressure contours (LGR-VL)

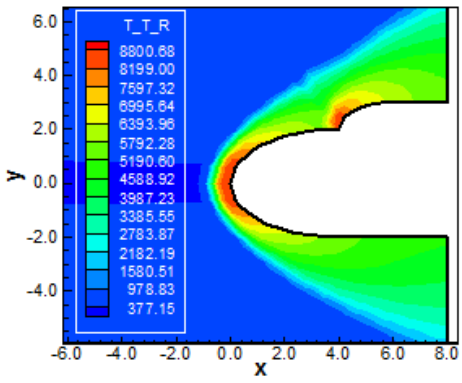

Fig. 48. Translational/rotational temperature contours (LGR-VL)

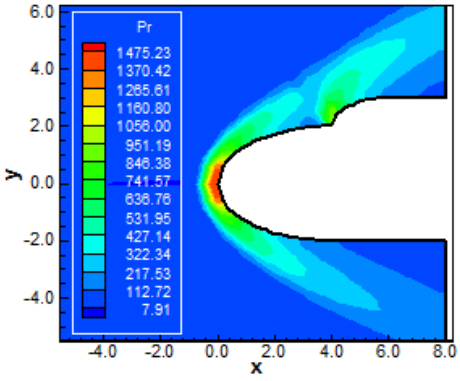

Fig. 49. Pressure contours (LGL-VL)

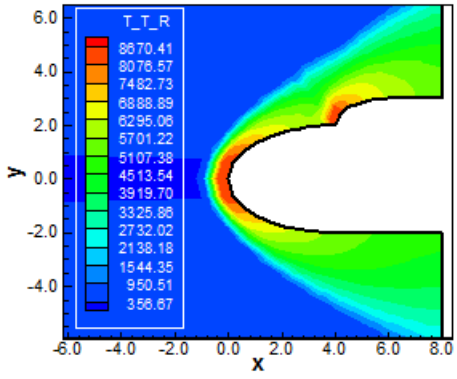

Fig. 50. Translational/rotational temperature contours (LGL-VL)

DOUBLE ELLIPSE VISCOUS SOLUTIONS

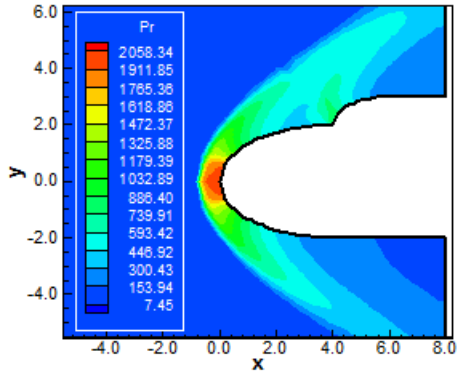

Fig. 51. Pressure contours (CGR-VL)

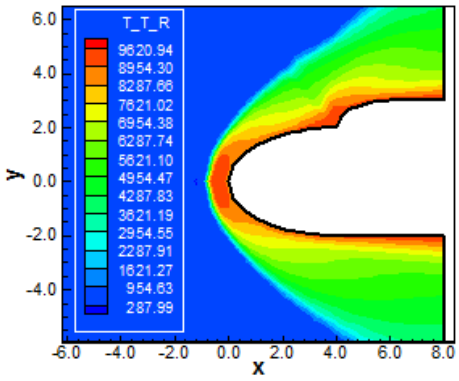

Fig. 52. Translational/rotational temperature contours (CGR-VL)

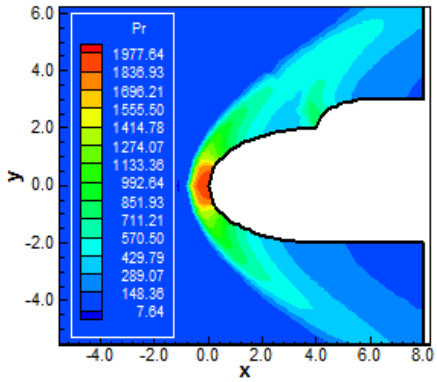

Fig. 53. Pressure contours (CGL-VL)

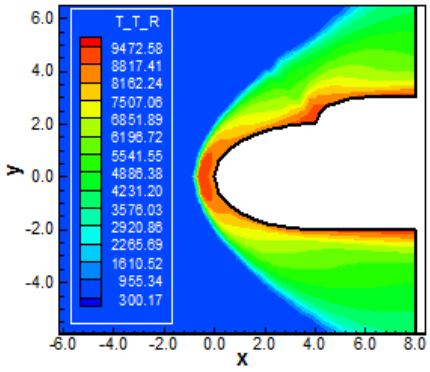

Fig. 54. Translational/rotational temperature contours (CGL-VL)

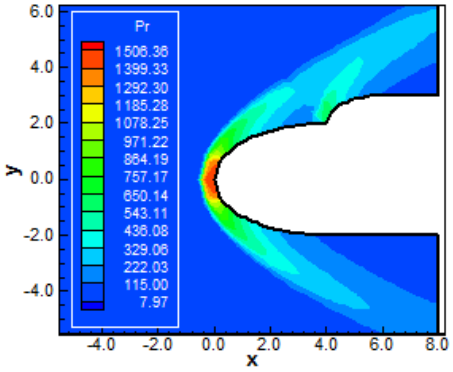

Fig. 55. Pressure contours (LGR-VL)

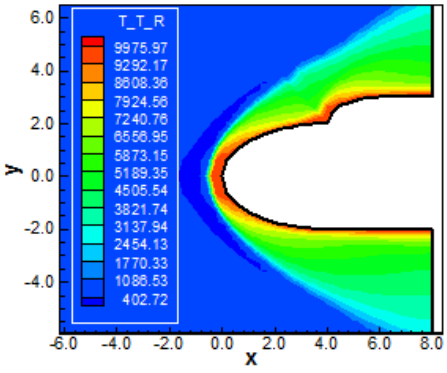

Fig. 56. Translational/rotational temperature contours (LGR-VL)

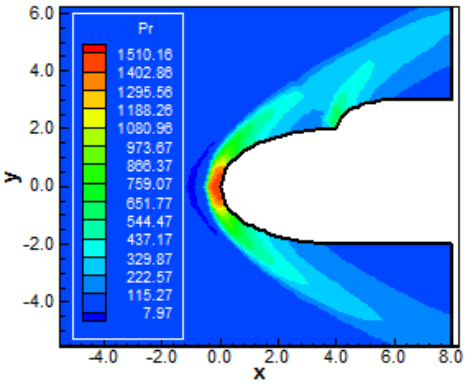

Fig. 57. Pressure contours (LGL-VL)

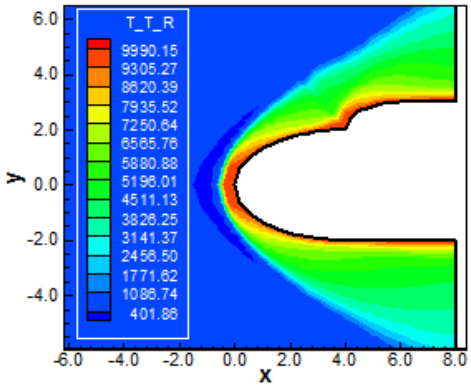

Fig. 58 Translational/rotational temperature contours (LGL-VL)

Figs. 63 to 66 show the pressure and temperature contours generated by the VL and LS numerical algorithms when using the CGL collocation points. There are some pre-shock oscillations in the VL solution, but good symmetry properties are observed in both solutions. The stagnation pressure estimated by the VL scheme as using CGL collocation points

is the best in comparison with the CGR, LGR, and LGL solutions, with an error of 3.88%. The temperature contours are shown in Figs. 65 and 66 and both figures present good symmetry characteristics, without oscillations.

REENTRY CAPSULE INVISCID SOLUTIONS

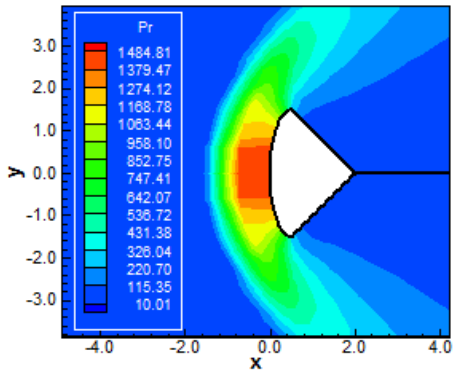

Fig. 59. Pressure contours (CGR-VL)

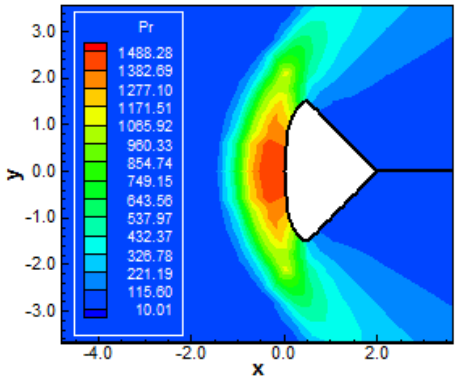

Fig. 60. Pressure contours (CGR-LS)

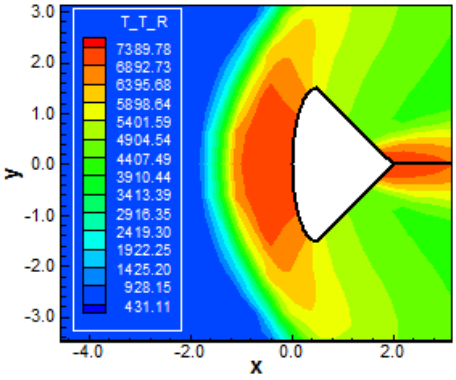

Fig. 61. Translational/rotational temperature contours (CGR-VL)

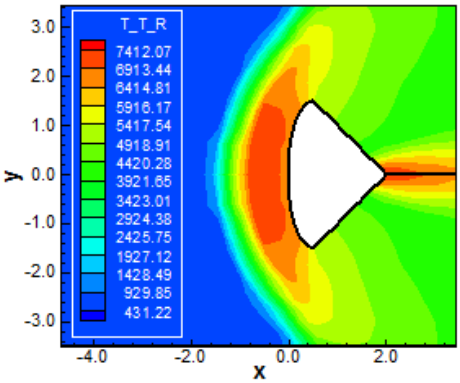

Fig. 62. Translational/rotational temperature contours (CGR-LS)

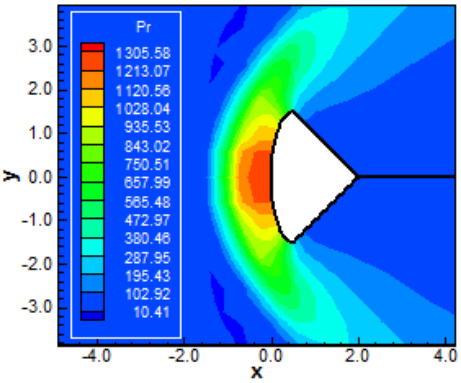

Fig. 63. Pressure contours (CGL-VL)

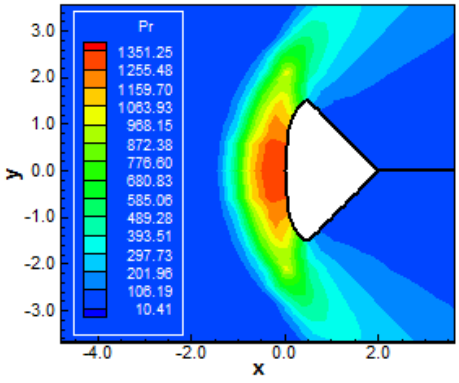

Fig. 64. Pressure contours (CGL-LS)

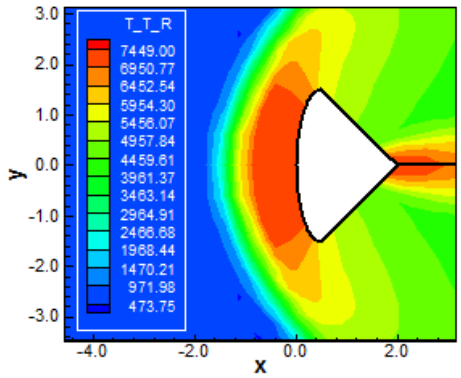

Fig. 65. Translational/rotational temperature contours (CGL-VL)

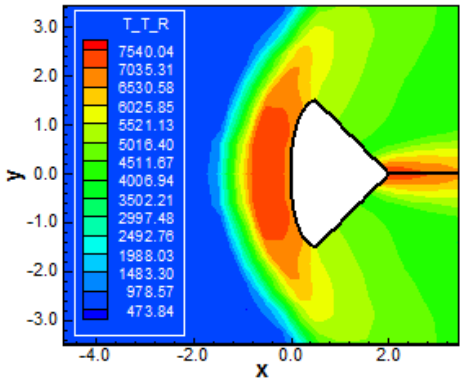

Fig. 66. Translational/rotational temperature contours (CGL-LS)

Figs. 67 to 70 exhibit the pressure and translational/rotational temperature contours calculated by the VL and LS algorithms as using the LGR collocation points. The values of stagnation pressure obtained by the numerical schemes are inferior to the theoretical value. As mentioned before, it seems that the Legendre variant behaves better for the temperature field and for the determination of the lift aerodynamic coefficient, as seen in Tables. 8 and 9. Good symmetry properties are observed in all solutions and free of oscillations.

Figs. 71 to 74 show the pressure and translational/rotational temperature contours obtained by the VL and LS schemes as using the LGL collocation points. Both schemes capture correctly the normal shock wave ahead of the configuration nose. Moreover, the stagnation pressure values of both schemes are under-predicted in relation to the theoretical value. Good symmetry properties are observed. Good homogenous properties are verified in the temperature solutions. The trailing edge flow is well captured by the numerical schemes, emphasizing the correct implementation of the Kutta condition.

Viscous case: Figs. 75 and 76 exhibit the pressure and temperature contours calculated by the VL numerical scheme as using the CGR collocation points. The LS scheme did not converge. Good symmetry properties are observed. The dynamic and thermal shock waves are correctly captured by the VL algorithm.

Figs. 77 to 80 show the pressure and translational/rotational temperature contours generated by the VL and LS schemes when using the CGL collocation points. The best result of the viscous case for the stagnation pressure was obtained by the CGL spectral variant with an error of 1.12%. Again, it seems that the Chebyshev variants present better behavior when applied to the dynamic part of the flow. Good symmetry properties are verified. Good homogenous properties are observed in both solutions.

Figs. 81 to 84 present the pressure and temperature contours obtained by the VL and LS numerical schemes as using the LGR collocation points. The stagnation pressure values generated by the VL and LS schemes are under-estimated in relation to the theoretical value. The contours are free of pre-shock oscillations and present good homogenous features. Figs. 83 and 84 present the temperature contours. The normal thermal shock wave is well captured by the numerical algorithms. Good symmetry properties are observed and the wake is well captured by the numerical schemes, highlighting the correct implementation of the Kutta condition.

Figs. 85 to 88 exhibit the pressure and temperature contours calculated by the VL and LS numerical algorithms when using the LGL collocation points. The stagnation pressure continues under-estimated. Good symmetry properties are verified. The temperature contours are free of oscillations, the wake is well captured by the numerical schemes, and good homogenous properties are noted. The normal thermal shock wave is well captured by the numerical schemes.

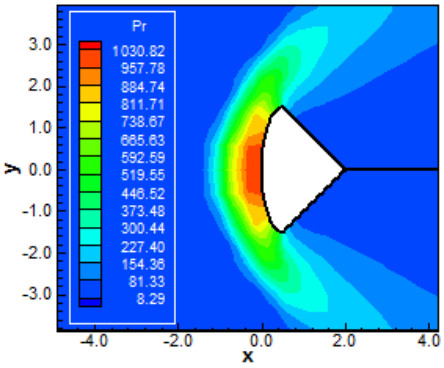

Fig. 67. Pressure contours (LGR-VL)

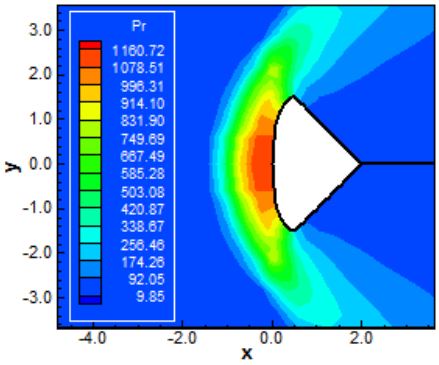

Fig. 68. Pressure contours (LGR-LS)

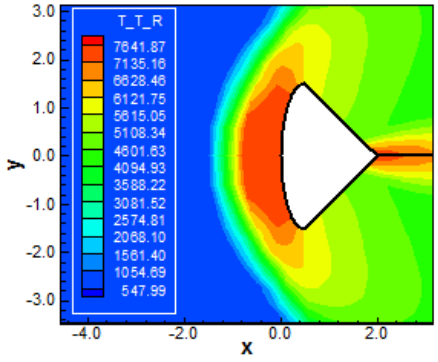

Fig. 69. Translational/rotational temperature contours (LGR-VL)

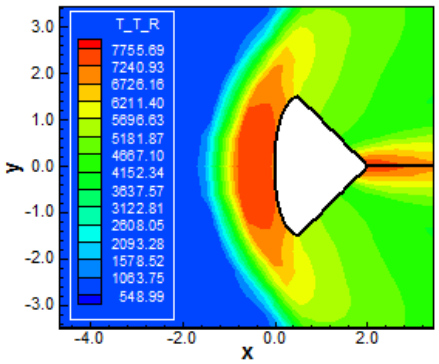

Fig. 70. Translational/rotational temperature contours (LGR-LS)

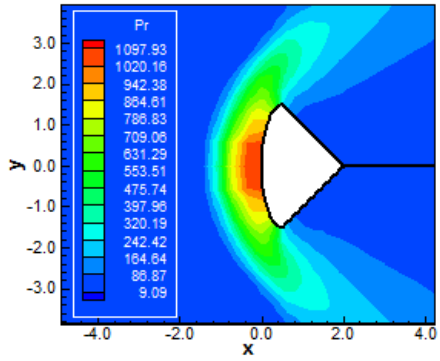

Fig. 71. Pressure contours (LGL-VL)

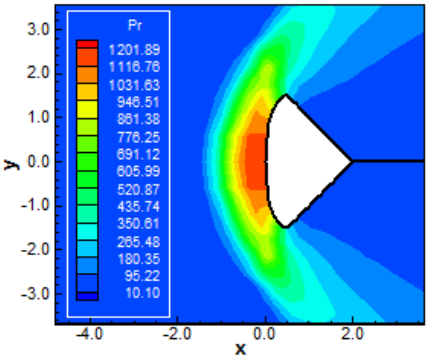

Fig. 72. Pressure contours (LGL-LS)

8.4 Other Comparisons

Figs. 89 and 90 show the convergence histories of the VL and LS schemes, respectively, for a 5th order spectral method using CGL for collocation points compared with two ENO solutions also of 5th order using Newton and Hermite interpolation functions, and a WENO solution also of 5th order, to the blunt body inviscid case. The CGL collocation points were chosen because they provide the best convergence for the inviscid case and 5th order of accuracy. The ENO and WENO schemes were implemented by the first author and they were used for numerical comparisons. To details of the implementation of the ENO and WENO schemes, the reader is encouraged to read [33-35]. As can be seen in Fig. 89, the Spectral (CGL) method coupled with

the VL scheme was the most efficient converging in less than 300 iterations, with a maximum CFL of 0.70. In second place, was the ENO (Hermite) interpolation function coupled with the VL scheme with a maximum CFL of 0.70, and converging in less than 300 iterations too. The ENO and WENO schemes used a maximum CFL number of 0.10 and were very inefficient. Fig. 90 compares the ENO solution of 5th order using Newton and Hermite interpolation functions, and the Spectral (CGL) method, all of them coupled with the LS scheme. In this case, the superiority of the Spectral (CGL) method was very highlighted, converging in less than 400 iterations, whereas the ENO (Hermite) converged in quasi 600 iterations.

Figs. 91 and 92 exhibit the convergence histories of the VL and LS schemes, respectively, for a 4th order spectral method using LGL for collocation points compared with a ENO solution also of 4th order using Newton interpolation function, to the blunt body viscous case. The LGL collocation points were chosen because they provide the best convergence for the viscous case and 4th order of accuracy. As can be seen in Fig. 91, the Spectral (LGL) method coupled with the VL scheme was the most efficient converging in less than 400 iterations, with a maximum CFL of 0.50. The ENO scheme used a maximum CFL number of 0.10 and was very inefficient. Fig. 92 compares the ENO solution of 4th order using Newton interpolation function, and the Spectral (LGL) method, both of them coupled with the LS scheme. In this case, the superiority of the Spectral (LGL) method was very highlighted, converging in less than 400 iterations, whereas the ENO (Newton) converged in more than 2,800 iterations.

As conclusion, the correct implementation of the proposed spectral method conducted to an efficient high order scheme, converging in less than 400 iterations in both inviscid and viscous cases, when programmed coupled with the VL or LS schemes. The CGL and LGL variants of the spectral method were the most efficient in the studies performed by the first author and ratified the fast convergence as expected.

8.5 Quantitative Analysis

In order to perform a quantitative analysis, the present reactive results are compared to the perfect gas solutions. The stagnation pressures at the blunt body nose, at the double ellipse nose, and at the reentry capsule nose were evaluated assuming the perfect gas formulation. Such parameters calculated at this way are not the best comparison, but in the absence of practical reactive results, these constitute the best available solution.

To calculate the stagnation pressure at the nose of these three configurations, [36] presents in its B Appendix values of the normal shock wave properties ahead of the configuration. The ratio pr_0/pr_∞ is estimated as function of the normal Mach number and the stagnation pressure pr_0 can be determined from this parameter. For the stagnation pressure, the value of pr_∞ is determined by the following expression:

$$\mathrm{pr}_\infty = \frac{\mathrm{pr}_{\mathrm{initial}}}{\rho_{\mathrm{char}} \times a^2_{\mathrm{char}}}, \tag{15}$$

where, for instance, to the blunt body case, $pr_{initial}$ = 687N/m^2, ρ_{char} = 0.004kg/m^3 and a_{char} = 317.024m/s. Considering these values, one concludes that pr_∞ = 1.709 (non-dimensional). Using the ratio obtained from [36], to an initial Mach number of 8.78, the ratio pr_0/pr_∞ assumes the value 99.98, the stagnation pressure ahead of the configuration nose is estimated as 170.87 unities.

Hence, Table 5 gives the theoretical stagnation pressure value obtained for the three configurations at the initial-normal-Mach number. Tables 6 (inviscid case) and 7 (viscous case) compare values of the stagnation pressure obtained from the simulations with the theoretical values and show the percentage errors. In the double ellipse problem, only the VL scheme generated converged results. As can be seen, the best results in the inviscid case are provided by the Chebyshev-Gauss-Radau collocation points, with an error of 5.96%, when using the LS scheme, for the blunt body problem; by the Chebyshev-Gauss-Radau collocation points, with an error of 3.79%, when using the VL scheme, for the double ellipse problem; and by Chebyshev-Gauss-Lobatto collocation points, with an error of 3.88%, when using the LS scheme, for the reentry capsule problem. For the viscous case, the Chebyshev-Gauss-Lobatto collocation points, with an error of 1.31%, using the LS scheme, for the blunt body problem, was the best; the Chebyshev-Gauss-Radau collocation points, with an error of 0.23%, using the VL scheme, for the double ellipse problem, was the best; and the Chebyshev-Gauss-Lobatto collocation points, with an error of 1.12%, using the LS scheme, for the reentry capsule problem, was the best.

As the hypersonic flows along the blunt body and along the reentry capsule configurations were simulated with a zero value to the attack angle and the geometries are symmetrical in relation to y axis, a zero lift coefficient is the expected value for this aerodynamic coefficient. Tables 8 (inviscid) and 9 (viscous) exhibit an analysis of the lift aerodynamic coefficient, based only on pressure contribution, for the blunt body and reentry capsule configurations, in this study. As can be observed, the best value to the lift coefficient in the inviscid case was obtained by the Legendre-Gauss-Radau collocation points, using VL scheme, for the blunt body problem; and again by the Legendre-Gauss-Radau collocation points, using VL scheme, for the reentry capsule problem. In the viscous case, the best value to the lift coefficient was obtained by the Legendre-Gauss-Lobatto collocation points, using LS scheme, for the blunt body problem; and by the Chebyshev-Gauss-Radau collocation points, using VL scheme, for the reentry capsule problem.

Table 1. Values of S_x and S_y

Surface	S_x	S_y
i,j-1/2	$\left(y_{i+1,j} - y_{i,j}\right)$	$\left(x_{i,j} - x_{i+1,j}\right)$
i+1/2,j	$\left(y_{i+1,j+1} - y_{i+1,j}\right)$	$\left(x_{i+1,j} - x_{i+1,j+1}\right)$
i,j+1/2	$\left(y_{i,j+1} - y_{i+1,j+1}\right)$	$\left(x_{i+1,j+1} - x_{i,j+1}\right)$
i-1/2,j	$\left(y_{i,j} - y_{i,j+1}\right)$	$\left(x_{i,j+1} - x_{i,j}\right)$

Table 2. Initial conditions to the blunt body problem

Property	Value
$M_{initial}$	8.78
$\rho_{initial}$	0.00326 kg/m^3
$pr_{initial}$	687 Pa
$U_{initial}$	4,776 m/s
$T_{initial}$	694 K
Altitude	40,000 m
c_N	10^{-9}
c_O	0.07955
c_{O2}	0.13400
c_{NO}	0.05090
L_{REF}	2.0 m
Re_{char}	2.386x10^6

8.6 Computational Performance

Tables 10 and 11 present the computational data of the VL and LS schemes for the blunt body, for the double ellipse, and for the reentry capsule problems in both inviscid and viscous cases, respectively. It shows the CFL number and the number of iterations to convergence for all studied cases in the current work. It can be verified that the best performance of the VL scheme in the inviscid case occurred when using the CGL collocation points, employing a CFL of 0.70, and converging in 239 iterations, in the blunt body problem, whereas in the viscous case occurred when using the LGL collocation points, employing a CFL of 0.30, and converging in 367 iterations, also in the blunt body problem. On the other hand, the best performance of the LS scheme in the inviscid case occurred when using the LGR collocation points, employing a CFL of 0.50, and converging in 320 iterations, in the blunt body problem, whereas in the viscous case occurred when using the LGR collocation points, employing a CFL of 0.30, and converging in 383 iterations, also in the blunt body problem.

Table 3. Initial conditions to the double ellipse problem

Property	Value
$M_{initial}$	15.0
$\rho_{initial}$	0.00922 kg/m^3
$pr_{initial}$	794 Pa
$U_{initial}$	5,208 m/s
$T_{initial}$	300 K
Altitude	50,000 m
c_N	10^{-9}
c_O	0.07955
c_{O2}	0.13400
c_{NO}	0.05090
L_{REF}	5.0 m
Re_{char}	1.574x10^6

Table 4. Initial conditions to the reentry capsule problem

Property	Value
$M_{initial}$	10.6
$\rho_{initial}$	0.02863 kg/m^3
$pr_{initial}$	3,885 Pa
$U_{initial}$	4,628 m/s
$T_{initial}$	473 K
Altitude	40,000 m
c_N	10^{-9}
c_O	0.07955
c_{O2}	0.13400
c_{NO}	0.05090
L_{REF}	3.0 m
Re_{char}	3.468x10^6

As final conclusion, it is possible to highlight that, for the blunt body problem, the LS scheme in the

viscous case using CGL collocation points had the best performance in estimating the stagnation pressure, and the lift aerodynamic coefficient was best estimated by the LS scheme as using the LGL collocation points; for the double ellipse problem, the VL scheme in the viscous case using CGR collocation points had the best performance in estimating the stagnation pressure; and finally, for the reentry capsule problem, the LS scheme in the viscous case using CGL collocation points had the best performance in estimating the stagnation pressure, and the lift aerodynamic coefficient was best estimated by the VL scheme as using the CGR collocation points. Moreover, the best performance of the numerical schemes, for the 4^{th} order of accuracy, was due to the VL one, when using the CGL collocation points, employing a CFL of 0.70, and converging in 239 iterations, in the blunt body problem, whereas for the 16^{th} order of accuracy, the best performance of the numerical schemes was due to the LS one, when using the LGR collocation points, employing a CFL of 0.30, and converging in 383 iterations, also in the blunt body problem.

Finally, to close this work, the computational cost of the numerical schemes using the several types of collocation points is presented in Table 12. For the inviscid case, the cheapest combination was the VL scheme using LGL collocation points with a cost of 0.00006974 sec/per-volume/per-iteration, whereas for the viscous case the cheapest was due to the LS scheme coupled with the LGR collocation points with a cost of 0.00017830 sec/per-volume/per-iteration.

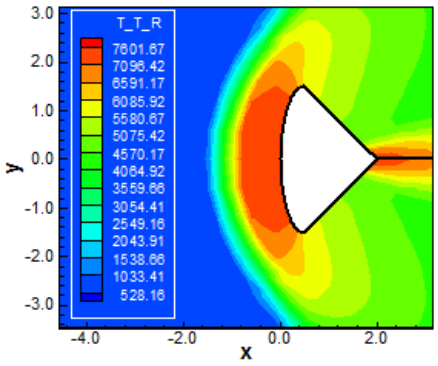

Fig. 73. Translational/rotational temperature contours (LGL-VL)

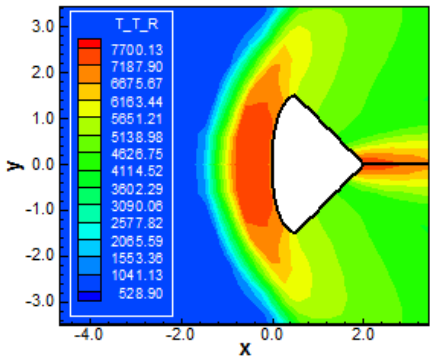

Fig. 74. Translational/rotational temperature contours (LGL-LS)

REENTRY CAPSULE VISCOUS SOLUTIONS

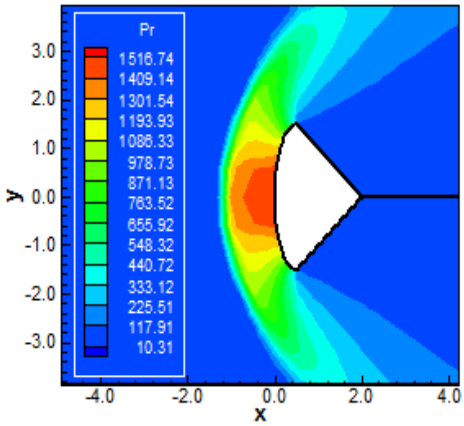

Fig. 75. Pressure contours (CGR-VL)

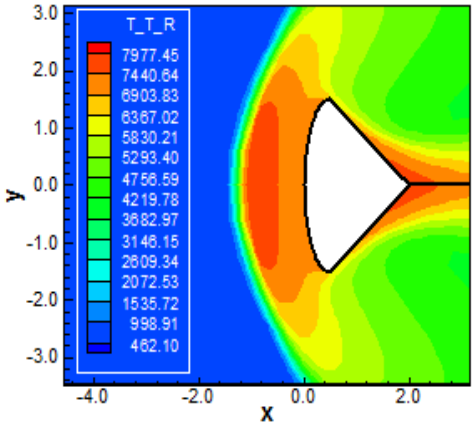

Fig. 76. Translational/rotational temperature contours (CGR-VL)

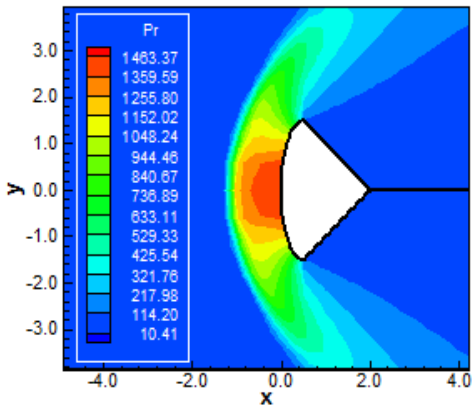

Fig. 77. Pressure contours (CGL-VL)

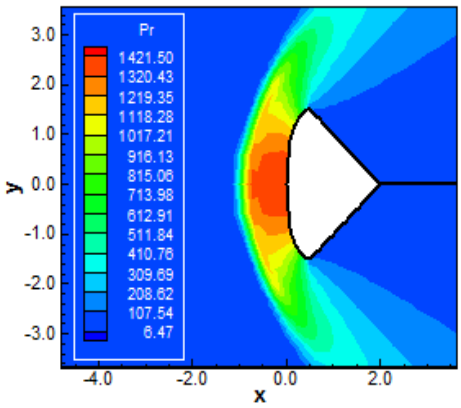

Fig. 78. Pressure contours (CGL-LS)

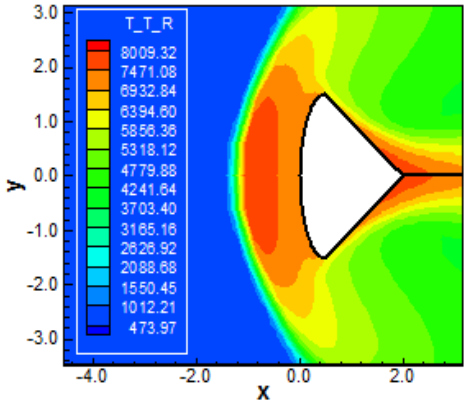

Fig. 79. Translational/rotational temperature contours (CGL-VL)

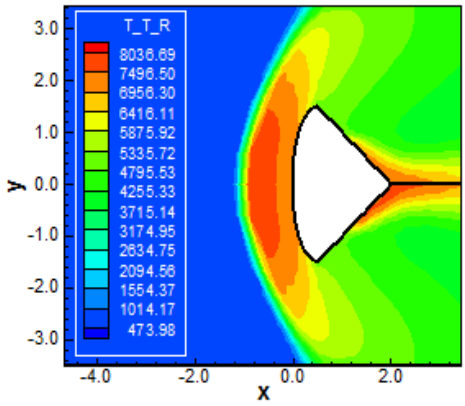

Fig. 80. Translational/rotational temperature contours (CGL-LS)

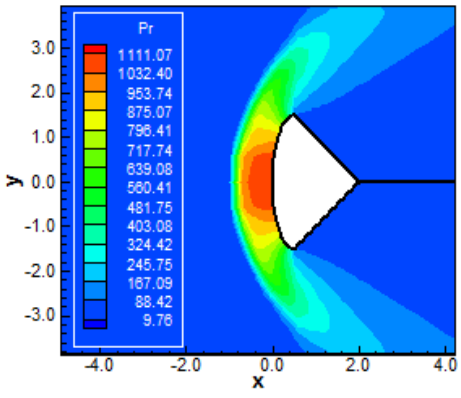

Fig. 81. Pressure contours (LGR-VL)

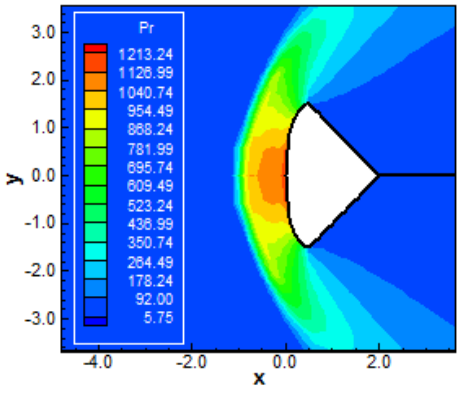

Fig. 82. Pressure contours (LGR-LS)

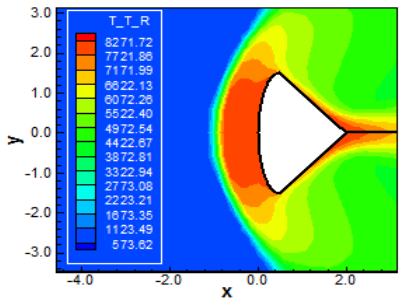

Fig. 83. Translational/rotational temperature contours (LGR-VL)

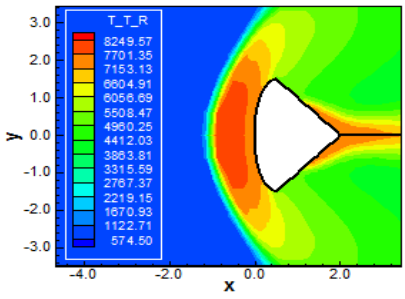

Fig. 84. Translational/rotational temperature contours (LGR-LS)

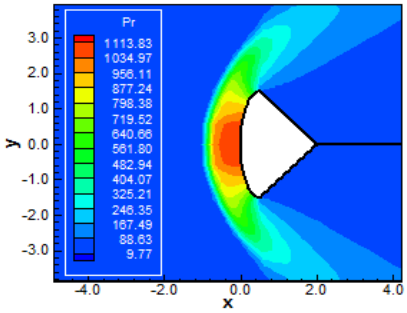

Fig. 85. Pressure contours (LGL-VL)

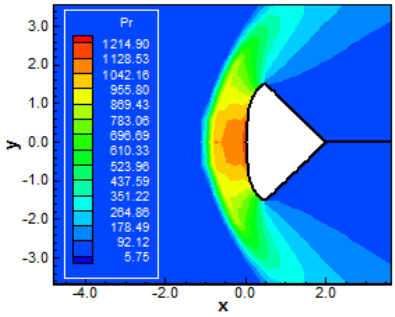

Fig. 86. Pressure contours (LGL-LS)

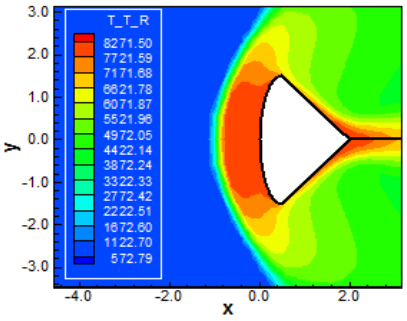

Fig. 87. Translational/rotational temperature contours (LGL-VL)

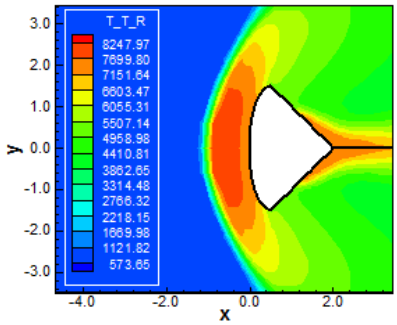

Fig. 88. Translational/rotational temperature contours (LGL-LS)

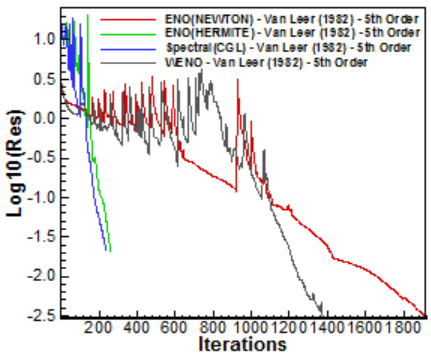

Fig. 89. Convergence histories – Inviscid case (VL)

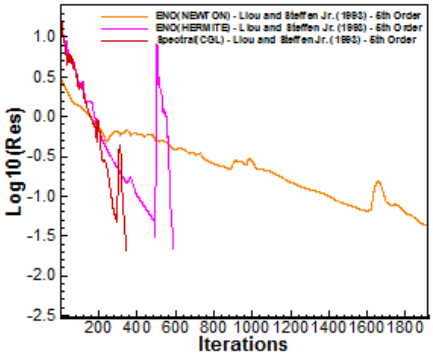

Fig. 90. Convergence histories – Inviscid case (LS)

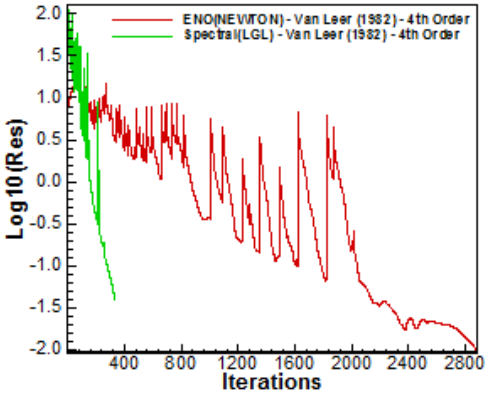

Fig. 91. Convergence histories – Viscous case (VL)

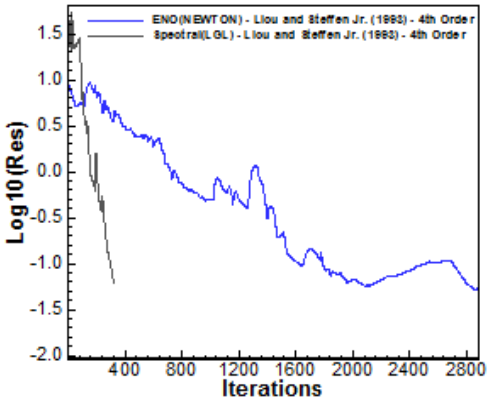

Fig. 92. Convergence histories – Viscous case (LS)

Table 5. Values of theoretical stagnation pressure

Problem:	$M_{initial}$:	pr_0/pr_∞:	pr_∞:	pr_0 (Theoretical):
Blunt body	8.78	99.98	1.709	170.87
Double ellipse	15.00	290.20	7.109	2,063.03
Reentry capsule	10.60	145.46	9.664	1,405.73

Table 6. Values of stagnation pressure and respective errors (Inviscid case/4th Order)

Physical problem:	Scheme:	Spectral method:	pr_0: (Numerical)	Error:
	VL(1)	Chebyshev-Gauss-Radau	139.22	18.52
	LS(2)	Chebyshev-Gauss-Radau	160.69	5.96
	VL	Chebyshev-Gauss-Lobatto	140.64	17.69
Blunt Body	LS	Chebyshev-Gauss-Lobatto	145.08	15.09
(pr_0 = 170.87)	VL	Legendre-Gauss-Radau	98.88	42.13
	LS	Legendre-Gauss-Radau	121.09	29.13
	VL	Legendre-Gauss-Lobatto	109.51	35.91
	LS	Legendre-Gauss-Lobatto	127.29	25.50
	VL	Chebyshev-Gauss-Radau	1,984.91	3.79
	LS	Chebyshev-Gauss-Radau	-	-
	VL	Chebyshev-Gauss-Lobatto	1,702.57	17.47
Double Ellipse	LS	Chebyshev-Gauss-Lobatto	-	-
(pr_0 = 2,063.03)	VL	Legendre-Gauss-Radau	1,372.91	33.45
	LS	Legendre-Gauss-Radau	-	-
	VL	Legendre-Gauss-Lobatto	1,475.23	28.49
	LS	Legendre-Gauss-Lobatto	-	-
	VL	Chebyshev-Gauss-Radau	1,484.81	5.63
	LS	Chebyshev-Gauss-Radau	1,488.28	5.87
	VL	Chebyshev-Gauss-Lobatto	1,305.58	7.12
Reentry Capsule	LS	Chebyshev-Gauss-Lobatto	1,351.25	3.88
(pr_0 = 1,405.73)	VL	Legendre-Gauss-Radau	1,030.82	26.67
	LS	Legendre-Gauss-Radau	1,160.72	17.43
	VL	Legendre-Gauss-Lobatto	1,097.93	21.90
	LS	Legendre-Gauss-Lobatto	1,201.89	14.50

(1): Van Leer; (2): Liou and Steffen Jr.

Table 7. Values of stagnation pressure and respective errors (Viscous case/16th Order)

Physical problem:	Scheme:	Spectral method:	pr_0: (Numerical)	Error:
	VL	Chebyshev-Gauss-Radau	184.50	7.98
	LS	Chebyshev-Gauss-Radau	176.56	3.33
	VL	Chebyshev-Gauss-Lobatto	177.23	3.72
Blunt Body	LS	Chebyshev-Gauss-Lobatto	173.10	1.31
(pr_0 = 170.87)	VL	Legendre-Gauss-Radau	131.98	22.76
	LS	Legendre-Gauss-Radau	145.46	14.87
	VL	Legendre-Gauss-Lobatto	132.32	22.56
	LS	Legendre-Gauss-Lobatto	145.67	14.75
	VL	Chebyshev-Gauss-Radau	2,058.34	0.23
	LS	Chebyshev-Gauss-Radau	-	-
	VL	Chebyshev-Gauss-Lobatto	1,977.64	4.14
Double Ellipse	LS	Chebyshev-Gauss-Lobatto	-	-
(pr_0 = 2,063.03)	VL	Legendre-Gauss-Radau	1,506.36	26.98
	LS	Legendre-Gauss-Radau	-	-
	VL	Legendre-Gauss-Lobatto	1,510.16	26.80
	LS	Legendre-Gauss-Lobatto	-	-
	VL	Chebyshev-Gauss-Radau	1,516.74	7.90
	LS	Chebyshev-Gauss-Radau	-	-
	VL	Chebyshev-Gauss-Lobatto	1,463.37	4.10
Reentry Capsule	LS	Chebyshev-Gauss-Lobatto	1,421.50	1.12
(pr_0 = 1,405.73)	VL	Legendre-Gauss-Radau	1,111.07	20.96
	LS	Legendre-Gauss-Radau	1,213.24	13.69
	VL	Legendre-Gauss-Lobatto	1,113.83	20.77
	LS	Legendre-Gauss-Lobatto	1,214.90	13.58

Table 8. Values of the lift aerodynamic coefficient (Inviscid case/4th Order)

Physical problem:	Scheme:	Spectral method:	c_L:
	VL	Chebyshev-Gauss-Radau	4.1766×10^{-14}
	LS	Chebyshev-Gauss-Radau	2.6970×10^{-14}
	VL	Chebyshev-Gauss-Lobatto	-2.2093×10^{-15}
Blunt Body	LS	Chebyshev-Gauss-Lobatto	-4.3648×10^{-14}
	VL	Legendre-Gauss-Radau	8.2827×10^{-16}
	LS	Legendre-Gauss-Radau	1.2645×10^{-14}
	VL	Legendre-Gauss-Lobatto	1.1761×10^{-14}
	LS	Legendre-Gauss-Lobatto	2.1764×10^{-14}
	VL	Chebyshev-Gauss-Radau	-2.1896×10^{-9}
	LS	Chebyshev-Gauss-Radau	9.4338×10^{-10}
	VL	Chebyshev-Gauss-Lobatto	-1.0423×10^{-9}
Reentry capsule	LS	Chebyshev-Gauss-Lobatto	4.6425×10^{-10}
	VL	Legendre-Gauss-Radau	4.3942×10^{-11}
	LS	Legendre-Gauss-Radau	-9.2069×10^{-11}
	VL	Legendre-Gauss-Lobatto	-5.3471×10^{-11}
	LS	Legendre-Gauss-Lobatto	5.6322×10^{-11}

Table 9. Values of the lift aerodynamic coefficient (Viscous case/16th Order)

Physical problem:	Scheme:	Spectral method:	c_L:
	VL	Chebyshev-Gauss-Radau	2.3130×10^{-15}
	LS	Chebyshev-Gauss-Radau	2.5299×10^{-14}
	VL	Chebyshev-Gauss-Lobatto	6.9929×10^{-15}
Blunt Body	LS	Chebyshev-Gauss-Lobatto	2.1638×10^{-14}
	VL	Legendre-Gauss-Radau	-8.9717×10^{-16}

Physical problem:	Scheme:	Spectral method:	c_L:
	LS	Legendre-Gauss-Radau	-2.0814×10^{-15}
	VL	Legendre-Gauss-Lobatto	8.4745×10^{-16}
	LS	Legendre-Gauss-Lobatto	1.6422×10^{-16}
	VL	Chebyshev-Gauss-Radau	-6.6822×10^{-12}
	LS	Chebyshev-Gauss-Radau	-
	VL	Chebyshev-Gauss-Lobatto	-1.1925×10^{-11}
Reentry Capsule	LS	Chebyshev-Gauss-Lobatto	1.5878×10^{-3}
	VL	Legendre-Gauss-Radau	-3.9489×10^{-11}
	LS	Legendre-Gauss-Radau	-1.4035×10^{-4}
	VL	Legendre-Gauss-Lobatto	-4.8359×10^{-11}
	LS	Legendre-Gauss-Lobatto	-1.3768×10^{-4}

Table 10. Computational data (Inviscid case/4th Order)

Physical problem:	Scheme:	Spectral method:	CFL:	Iterations:
	VL	Chebyshev-Gauss-Radau	0.70	404
	LS	Chebyshev-Gauss-Radau	0.70	378
	VL	Chebyshev-Gauss-Lobatto	0.70	239
Blunt Body	LS	Chebyshev-Gauss-Lobatto	0.70	344
	VL	Legendre-Gauss-Radau	0.50	241
	LS	Legendre-Gauss-Radau	0.50	320
	VL	Legendre-Gauss-Lobatto	0.50	242
	LS	Legendre-Gauss-Lobatto	0.50	352
	VL	Chebyshev-Gauss-Radau	0.10	2,987
	LS	Chebyshev-Gauss-Radau	-	-
	VL	Chebyshev-Gauss-Lobatto	0.20	974
Double Ellipse	LS	Chebyshev-Gauss-Lobatto	-	-
	VL	Legendre-Gauss-Radau	0.20	519
	LS	Legendre-Gauss-Radau	-	-
	VL	Legendre-Gauss-Lobatto	0.20	590
	LS	Legendre-Gauss-Lobatto	-	-
	VL	Chebyshev-Gauss-Radau	0.30	1,027
	LS	Chebyshev-Gauss-Radau	0.30	1,122
	VL	Chebyshev-Gauss-Lobatto	0.30	814
Reentry Capsule	LS	Chebyshev-Gauss-Lobatto	0.30	917
	VL	Legendre-Gauss-Radau	0.10	1,748
	LS	Legendre-Gauss-Radau	0.10	2,791
	VL	Legendre-Gauss-Lobatto	0.10	2,819
	LS	Legendre-Gauss-Lobatto	0.10	3,077

Table 11. Computational data (Viscous case/16th Order)

Physical problem:	Scheme:	Spectral method:	CFL:	Iterations:
	VL	Chebyshev-Gauss-Radau	0.50	560
	LS	Chebyshev-Gauss-Radau	0.50	506
	VL	Chebyshev-Gauss-Lobatto	0.50	501
Blunt Body	LS	Chebyshev-Gauss-Lobatto	0.50	468
	VL	Legendre-Gauss-Radau	0.30	432
	LS	Legendre-Gauss-Radau	0.30	383
	VL	Legendre-Gauss-Lobatto	0.30	367
	LS	Legendre-Gauss-Lobatto	0.30	386
	VL	Chebyshev-Gauss-Radau	0.05	11,203
	LS	Chebyshev-Gauss-Radau	-	-
	VL	Chebyshev-Gauss-Lobatto	0.10	4,914
Double Ellipse	LS	Chebyshev-Gauss-Lobatto	-	-
	VL	Legendre-Gauss-Radau	0.08	3,208

Physical problem:	Scheme:	Spectral method:	CFL:	Iterations:
	LS	Legendre-Gauss-Radau	-	-
	VL	Legendre-Gauss-Lobatto	0.08	3,105
	LS	Legendre-Gauss-Lobatto	-	-
	VL	Chebyshev-Gauss-Radau	0.10	4,435
	LS	Chebyshev-Gauss-Radau	-	-
	VL	Chebyshev-Gauss-Lobatto	0.10	3,986
Reentry Capsule	LS	Chebyshev-Gauss-Lobatto	0.10	4,052
	VL	Legendre-Gauss-Radau	0.09	2,012
	LS	Legendre-Gauss-Radau	0.10	2,410
	VL	Legendre-Gauss-Lobatto	0.09	2,023
	LS	Legendre-Gauss-Lobatto	0.10	2,422

Table 12. Computational cost of spectral variants

Order of accuracy:	Scheme:	Spectral method:	Computational cost (Seconds/volumes/iterations):
	VL	Chebyshev-Gauss-Radau	0.00007092
	LS	Chebyshev-Gauss-Radau	0.00007164
	VL	Chebyshev-Gauss-Lobatto	0.00007061
4^{th} Order	LS	Chebyshev-Gauss-Lobatto	0.00007073
(Inviscid case)	VL	Legendre-Gauss-Radau	0.00007002
	LS	Legendre-Gauss-Radau	0.00006991
	VL	Legendre-Gauss-Lobatto	0.00006974
	LS	Legendre-Gauss-Lobatto	0.00007024
	VL	Chebyshev-Gauss-Radau	0.00018502
	LS	Chebyshev-Gauss-Radau	0.00018150
	VL	Chebyshev-Gauss-Lobatto	0.00017939
16^{th} Order	LS	Chebyshev-Gauss-Lobatto	0.00018114
(Viscous case)	VL	Legendre-Gauss-Radau	0.00017988
	LS	Legendre-Gauss-Radau	0.00017830
	VL	Legendre-Gauss-Lobatto	0.00018073
	LS	Legendre-Gauss-Lobatto	0.00018505

9. CONCLUSIONS

In the present work, a study involving a spectral method to solve the reactive Euler and Navier-Stokes equations was performed. The Euler and Navier-Stokes equations, in conservative and finite volume contexts, employing structured spatial discretization, on a condition of chemical non-equilibrium, were studied. The spectral method presented in this work employed collocation points and variants of Chebyshev and Legendre interpolation functions were analyzed. High-order studies were performed to verify the accuracy of the spectral method. The “hot gas” hypersonic flows around a blunt body, around a double ellipse, and around a reentry capsule in two-dimensions were performed. The [19-20] flux vector splitting algorithms were applied to accomplish the numerical experiments. The Euler backward integration method was employed to march the schemes in time. The convergence process was accelerated to steady state condition through a spatially variable time step procedure, which has proved effective gains in terms of computational acceleration (see [21-22]). The reactive simulations involved Earth atmosphere chemical model of five species and seventeen reactions, based on the [23] model. N, O, N_2, O_2, and NO species were used to perform the numerical comparisons. The results have indicated that the Chebyshev collocation point variants are more accurate in terms of stagnation pressure estimations, whereas the Legendre collocation point variants are more accurate in terms of the lift coefficient estimations. Moreover, the Legendre collocation point variants are more computationally efficient and cheaper.

As final conclusion, it is possible to highlight that, for the blunt body problem, the [20] scheme in the viscous case using Chebyshev-Gauss-Lobatto collocation points had the best performance in estimating the stagnation pressure, and the lift aerodynamic coefficient was best estimated by the [20] scheme as using the Legendre-Gauss-Lobatto collocation points;

for the double ellipse problem, the [19] scheme in the viscous case using Chebyshev-Gauss-Radau collocation points had the best performance in estimating the stagnation pressure; and finally, for the reentry capsule problem, the [20] scheme in the viscous case using Chebyshev-Gauss-Lobatto collocation points had the best performance in estimating the stagnation pressure, and the lift aerodynamic coefficient was best estimated by the [19] scheme as using the Chebyshev-Gauss-Radau collocation points. Moreover, the best performance of the numerical schemes, for the 4^{th} order of accuracy, was due to the [19] one, when using the Chebyshev-Gauss-Lobatto collocation points, employing a CFL of 0.70, and converging in 239 iterations, in the blunt body problem, whereas for the 16^{th} order of accuracy, the best performance of the numerical schemes was due to the [20] one, when using the Legendre-Gauss-Radau collocation points, employing a CFL of 0.30, and converging in 383 iterations, also in the blunt body problem.

Finally, to close this work, the computational cost of the numerical schemes using the several types of collocation points was presented in Tab. 12, for a Core i7 processor of 2.1GHz and 8.0Gbytes of RAM microcomputer, in a Windows 7.0 environment. For the inviscid case, the cheapest combination was the VL scheme using Legendre-Gauss-Lobatto collocation points with a cost of 0.00006974 sec/per-volume/per-iteration, whereas for the viscous case the cheapest was due to the LS scheme coupled with the Legendre-Gauss-Radau collocation points with a cost of 0.00017830 sec/per-volume/per-iteration.

10. MOTIVATION AND NOVELTY

The motivation to study spectral methods applied to reentry flow was enormous because of some papers in the CFD literature reporting for such methods as the state of art of high order resolution. The intention of this paper was to propose a different spectral method that was of easy implementation and conformed about first author's ideas of treating the governing equations of fluid flow. The formulation presented here is for a chemical non-equilibrium condition and a one-temperature model. The comparisons involving the residual histories of ENO, WENO, and spectral method were very important to confirm that our numerical implementation was correct and also the potentiality of the method. Three physical problems were also a challenge that we accept to lead with. The results with good accuracy represent a motivation to extend the present formulation to more species and different chemical conditions.

The novelty of the present study was to implement this different spectral method to treat chemical non-equilibrium reentry flows and to formulate the appropriate equations for accept this method. The robustness and convergence features of this spectral method are very impressive. While the first author had to use CFL numbers of order 0.10 for his ENO/WENO explicit methods, CFL numbers as great as 0.70 for his explicit spectral method were of common use. The proposed spectral method is different from the standard spectral ones on a sense that in the latter, the differential equations and the solution method are discretized with spectral tools, whereas in the former, only the vector of conserved variables and the convective fluxes should be discretized according to the spectral tools. The result is a robust and fast solver to treat the fluid-dynamic of reentry flows.

11. FUTURE WORKS

For the future, the authors should extend the present formulation for a five species chemical model under the condition of thermochemical non-equilibrium in two-dimensions. After that, they should extend to seven and eleven species in two-dimensions until to arrive to the desired three-dimensional studies. Moreover, its implementation with turbulence effects and magnetic field actuation, that the first author consider as the state of the art project, is an objective to be reached, in both, two- and three-dimensions. For the cases where turbulence will be studied, the authors will follow the formulation described in [37-40], and for the magnetic field actuation the works of [39-43] will be employed. Finally, the interpretation of the present formulation to two-dimensional unstructured studies is also a goal to be reached.

ACKNOWLEDGEMENTS

The first author would like to thank the ITA facilities that allowed the realization of this work. He would also like to thank the CAPES by the financial support conceded under the form of a scholarship.

COMPETING INTERESTS

Authors have declared that no competing interests exist.

REFERENCES

1. Barnes CJ, Huang GP, Shang JS. A high resolution spectral method for the compressible Navier-Stokes equations. AIAA Paper 2011-49; 2011.
2. Huang P, Wang ZJ, Liu Y. An implicit space-time spectral difference method for discontinuity capturing using adaptive polynomials. AIAA Paper 2005-5255; 2005.
3. Huang P. High order discontinuity capturing using adaptive polynomials. AIAA Paper 2006-305; 2006.
4. Steger JL, Warming RF. Flux vector splitting of the Inviscid Gasdynamic Equations with application to finite difference methods. Journal of Computational Physics. 1981;40:263-293.
5. Hughes T. The finite element method, Linear Static and Dynamic Finite Element Analysis, Prentice-Hall, Inc.
6. Lele S. Compact finite difference schemes with spectral-like resolution. Journal of Computational Physics. 1991;103:16-42.
7. Gottlieb D, Orszag S. Numerical analysis of spectral methods: Theory and applications. Society for Industrial and Applied Mathematics, Philadelphia.
8. Hussaini MY, Kopriva DA, Salas MD, Zang TA. Spectral methods for the euler equations: Part I – Fourier methods and shock capturing. AIAA Journal. 1985;23(1): 64-70.
9. Slater JC. Electronic energy bands in metal. Physical Review. 1934;45:794-801.
10. Barta J. Ü ber die Naherungsweise L ü sung einiger Zweidimensionaler Elastizit ä tsaufgaben. Zeitschrift fuer Angewandte Mathematik und Mechanik. 1937;17:184-185.
11. Frazer RA, Jones WP, Skan SW. Approximation to functions and to the solutions of differential equations. Aeronautical Research Council, London, R&M 1799; 1937.
12. Lanczos CL. Trigonometric interpolation of empirical and analytic functions. Journal of Mathematics and Physics. 1938;17:123-199.
13. Gottlieb D, Lustman L, Orszag SA. Spectral calculations of one-dimensional inviscid compressible flows. SIAM Journal of Scientific and Statistical Computation. 1981;2:296-310.
14. Taylor TD, Meyers RB, Albert JH. Pseudospectral calculations of shock waves, rarefaction waves and contact surfaces. Computers and Fluids. 1981;9: 469-473.
15. Zang TA, Hussaini MY. Mixed spectral-finite difference approximations for slightly viscous flows. Proceedings of the 7th International Conference on Numerical Methods in Fluid Dynamics, edited by W. C. Reynolds and R. W. MacCormack, Lecture Notes in Physics, No. 141, Springer-Verlag, New York. 1981;461-466.
16. Narayan JR, Girimaji SS. Turbulent reacting flow computations including turbulence-chemistry interactions. AIAA Paper 92-0342; 1992.
17. Gnoffo PA, Gupta RN, Shinn JL. Conservation equations and physical models for hypersonic flows in thermal and chemical nonequilibrium. NASA TP 2867; 1989.
18. Liu M, Vinokur M. Upwind algorithms for general thermo-chemical nonequilibrium flows. AIAA Paper 89-0201; 1989.
19. Van Leer B. Flux-vector splitting for the Euler equations. Lecture Notes in Physics, Springer Verlag, Berlin. 1982;170:507-512.
20. Liou M, Steffen Jr. CJ. A new flux splitting scheme. Journal of Computational Physics. 1993;107:23-39.
21. Maciel ESG. Simulations in 2D and 3D applying unstructured algorithms, Euler and Navier-stokes equations – Perfect gas formulation, Saarbrücken, Deutschland: Lambert Academic Publishing (LAP). 2015; Ch. 1:26-47.
22. Maciel ESG. Simulations in 2D and 3D applying unstructured algorithms, Euler and Navier-stokes equations – Perfect Gas Formulation, Saarbrücken, Deutschland: Lambert Academic Publishing (LAP). 2015; Ch. 6:160-181.
23. Saxena SK, Nair MT. An improved roe scheme for real gas flow. AIAA Paper 2005-587; 2005.
24. Hussaini MY, Streett CL, Zang TA. Spectral methods for partial differential equations. ICASE Report No. 83-46; 1983.
25. Davis PA, Rabinowitz P. Numerical integration. Blaisdell Publishing Co.; 1967.
26. Canuto C, Hussaini MY, Quarteroni A, Zang TA. Spectral methods evolution to complex geometries and applications to fluid dynamics. Scientific Computation Springer; 2007.

27. Maciel ESG. Hypersonic reactive flow simulations in two-dimensions, chemical and thermochemical non-equilibrium conditions. Saarbrücken. Deutschland: Lambert Academic Publishing (LAP). 2015; Ch. 1:27-81.
28. Maciel ESG. Hypersonic reactive flow simulations in two-dimensions, chemical and thermochemical non-equilibrium conditions. Saarbrücken. Deutschland: Lambert Academic Publishing (LAP). 2015; Ch. 2:82-173.
29. Ait-Ali-Yahia D, Habashi WG. Finite element adaptive method for hypersonic thermochemical nonequilibrium flows. AIAA Journal. 1997;35(8):1294-1302.
30. Long LN, Khan MMS, Sharp HT. Massively parallel three-dimensional Euler / Navier-stokes method. AIAA Journal. 1991;29(5): 657-666.
31. Fox RW, McDonald AT. Introdução à Mecânica dos Fluidos. Guanabara Editor; 1988.
32. Maciel ESG. Simulação numérica de escoamentos supersônicos e hipersônicos utilizando técnicas de dinâmica dos fluidos computacional. Doctoral Thesis, ITA, CTA, São José dos Campos, SP, Brazil; 2002.
33. Maciel ESG. Comparison among MUSCL, ENO and WENO procedures as applied to reentry flows in 2D. Computational and Applied Mathematics Journal. 2015;1(5): 355-377.
34. Maciel ESG. High order resolution applied to chemical non-equilibrium reentry flows in 2D. Engineering and Technology. 2015; 2(5):256-275.
35. Maciel ESG. Comparison between Newton and Hermite ENO interpolations as applied to reentry flows in 2D. Computational and Applied Mathematics Journal. 2015;1(5): 261-281.
36. Anderson Jr. JD. Fundamentals of aerodynamics. McGraw-Hill, Inc., 5th Edition. 2010;1008.
37. Maciel ESG, Andrade CR. Turbulent chemical non-equilibrium reentry flows in 2D - five species. Asian Journal of Mathematics and Computer Research. 2017;20(3):130-168.
38. Maciel ESG, Andrade CR. Turbulent thermochemical non-equilibrium reentry flows in 2D - Eleven species. Asian Journal of Mathematics and Computer Research. 2017;20(4):179-217.
39. Maciel ESG, Andrade CR. CFD computations in two- and three-dimensions. Republic of Moldova: Lambert Academic Publishing (LAP). 2017;1-244.
40. Maciel ESG, Andrade CR. CFD applications in two- and three-dimensions. Republic of Moldova: EAE - Editorial Académica Española. 2017;1-244.
41. Maciel ESG. Magnetic field applied to thermochemical non-equilibrium reentry flows in 2D - Five species. International Journal of Computational Fluid Dynamics. 2015;1:1-24.
42. Maciel ESG, Andrade CR. Magnetic field applied to thermochemical non-equilibrium reentry flows in 2D - Seven species. International Journal of Applied Physics. 2016;6(2):117-172.
43. Maciel ESG, Andrade CR. Magnetic field in reentry flows in 2D: Eleven species. Journal of Advances in Mathematics and Computer Science. 2017;24(6):1-36.

Peer-review history:
The peer review history for this paper can be accessed here:
http://sciencedomain.org/review-history/21788